The Astrophysical Journal, 993:230 (23pp), 2025 November 10 https://doi.org/10.3847/1538-4357/ae06a0

Marvelous Metals: Surveying the Circumgalactic Medium of Simulated Dwarf Galaxies

Daniel R. Piacitelli[1], Alyson M. Brooks[1,2], Charlotte Christensen[3], N. Nicole Sanchez[4,5], Yakov Faerman[6,7], Sijing Shen[8], Akaxia Cruz[2], Ben Keller[9], Thomas R. Quinn[6], and James Wadsley[10]
[1] Department of Physics and Astronomy, Rutgers University, Piscataway, NJ 08854, USA; piacitelli.danielr@gmail.com
[2] Center for Computational Astrophysics, Flatiron Institute, 162 Fifth Avenue, New York, NY 10010, USA
[3] Physics Department, Grinnell College, 1116 Eighth Avenue, Grinnell, IA 50112, USA
[4] Carnegie Observatories, 813 Santa Barbara Street, Pasadena, CA 91101, USA
[5] California Institute of Technology, TAPIR 350-17, 1200 E. California Boulevard, Pasadena, CA 91125-0001, USA
[6] Department of Astronomy, University of Washington, Seattle, WA 98195, USA
[7] School of Physics and Astronomy, Tel Aviv University, Tel Aviv 69978, Israel
[8] Institute of Theoretical Astrophysics, University of Oslo, PO Box 1029, Blindern 0315, Oslo, Norway
[9] Department of Physics and Materials Science, University of Memphis, 3720 Alumni Avenue, Memphis, TN 38152, USA
[10] Department of Physics & Astronomy, McMaster University, ABB-241, 1280 Main Street West, Hamilton, ON L8S 4M1, Canada
Received 2025 May 13; revised 2025 September 11; accepted 2025 September 12; published 2025 November 6

Abstract

Dwarf galaxies are uniquely sensitive to feedback processes and known to experience substantial mass and metal loss from their disks. Here, we investigate the circumgalactic medium (CGM) of 64 isolated dwarf galaxies ($6.0 < \log(M_*/M_\odot) < 9.5$) at $z = 0$ from the Marvel-ous Dwarfs and Marvelous Massive Dwarfs simulations. Our galaxies produce column densities broadly consistent with current observations. We investigate these column densities in the context of mass and metal retention rates, and CGM physical properties. We find 48% ± 11% of all baryons within R_{200c} reside in the CGM, with ∼70% of CGM mass existing in a warm gas phase, $10^{4.5} < T < 10^{5.5}$ K, that dominates beyond $r/R_{200c} \sim 0.5$. The warm and cool ($10^{4.0} < T < 10^{4.5}$ K) gas phases each retain 5%–10% of metals formed by the dwarf galaxy. The significant fraction of mass and metals residing in the warm CGM phase provides an interpretation for the lack of $z \sim 0$ low ion detections beyond $b/R_{200c} \sim 0.5$, as the majority of mass in this region exists in higher ions. We find a weak correlation between galaxy mass and total CGM metal retention despite the fraction of metals lost from the halo increasing from ∼10% to >40% toward lower masses. Our findings highlight the CGM (particularly its warm phase) as a key reservoir of mass and metals for dwarf galaxies across stellar masses, underscoring its importance in understanding the baryon cycle in the low-mass regime. Finally, we provide individual simulated galaxy properties and quantify the fraction of UV-observable mass to support future observational programs aimed at performing a metal budget around dwarf galaxies.

Unified Astronomy Thesaurus concepts: Hydrodynamical simulations (767); Circumgalactic medium (1879); Dwarf galaxies (416); Stellar feedback (1602)

1. Introduction

Across galaxy masses, feedback processes are expected to play a key role in shaping galaxy evolution. For low-mass galaxies, the shallower gravitational wells result in stellar feedback processes being highly efficient at driving metal-enriched mass loss from the disk of the galaxy, thereby regulating star formation (e.g., B. W. Keller et al. 2016). Some observational estimates indicate that up to 95% of the metals produced by a dwarf galaxy's stellar population may no longer reside in its disk (e.g., K. B. W. McQuinn et al. 2015). However, the final fate of the ejected mass and metals remains an open question. Specifically, to answer these questions, it is essential to constrain the fraction of ejected mass and metals that escape into the intergalactic medium (IGM) and how much remains within the halo. In this direction, the circumgalactic medium of dwarf galaxies (hereafter CGM-DG) and its mass and metal content are key in understanding the galactic baryon cycle in the low-mass regime.

A growing number of observational studies have sought to map the distribution of the material in the CGM-DG. Out to $z \sim 0.7$, the CGM of isolated dwarf galaxies has been commonly detected in H I absorption (C. J. Liang & H.-W. Chen 2014; S. D. Johnson et al. 2017; R. Bordoloi et al. 2018; N. Mishra et al. 2024; Y. Zheng et al. 2024). In fact, H I detections have reached well beyond the virial radius of the galaxy, and equivalent width or column densities show a declining profile with increasing impact parameter from the galaxy (e.g., C. J. Liang & H.-W. Chen 2014; S. D. Johnson et al. 2017; N. Mishra et al. 2024).

Despite the common detections of H I, studies targeting metal absorption in the CGM-DG have yielded mixed results. Low-z studies have only successfully detected metal ions (C II, C IV, Si II, Si III, and Si IV) within the inner CGM ($\sim 0.5R_{\rm vir}$), but only nondetections (upper limits) have been found in the outer CGM and beyond (R. Bordoloi et al. 2014; C. J. Liang & H.-W. Chen 2014; J. N. Burchett et al. 2016; S. D. Johnson et al. 2017; Z. Qu & J. N. Bregman 2022; Y. Zheng et al. 2024). Similarly, at higher redshifts, detections of lower metal ions like C II, Si II, and Si III have been constrained within $r < 0.5R_{\rm vir}$ (e.g., N. Mishra et al. 2024). These low detection rates may suggest that the mass of metal-enriched gas declines significantly beyond $r \sim 0.5R_{\rm vir}$. However, at higher redshifts ($0.077 < z < 0.73$), O VI has been detected around dwarf galaxies out to twice their virial radius (S. D. Johnson et al. 2017; K. Tchernyshyov et al. 2022; N. Mishra et al. 2024;

Z. Qu et al. 2024). Since O VI is expected to exist in warmer conditions and lower ions in cooler conditions, these detections and nondetections imply that there is a cool component in the CGM-DG that is largely concentrated to the inner regions of the halo and a warm, extended component in the outer regions of the halo.

Additionally, observational studies have sought to quantify the mass and metals residing in the cool and warm phases of the CGM-DG. Y. Zheng et al. (2024) introduce empirical models for the CGM mass distribution that adopt gas density and volume filling factor values based on observed H I column densities. Utilizing these models, Y. Zheng et al. (2024) estimate the cool CGM phase ($T \sim 10^4$ K) around $M_* = 10^{8.3} M_\odot$ galaxies contains a mass of $M_{\rm CGM,cool} \sim 10^{8.4} M_\odot$—which only accounts for ∼2% of the galaxy's baryonic budget relative to the cosmic abundance ($f_{\rm CGM,cool} = M_{\rm CGM,cool}/M_{200m}\Omega_b/\Omega_m$). Recently, Y. Faerman et al. (2025) used existing H I column densities to derive a power-law density profile for the CGM-DG and provide observationally motivated constraints on the cool gas mass in the CGM-DG. They find that measured H I columns suggest <10% of the halo baryon budget resides in the cool, photoionized phase.

Regarding metal content, S. D. Johnson et al. (2017) estimate that the cool phase ($T \sim 10^4$ K) harbors only 2%–6% of the silicon budget, based on expected supernovae (SNe) yields. Similarly, Y. Zheng et al. (2024) predict that the cool phase contains ∼10% of the metals ever produced by the dwarf galaxy's star formation history. For the warmer, O VI-traced phase of the CGM-DG, studies have predicted a O VI mass of $M_{\rm CGM,O\ VI} \sim 10^{5.0–6.0} M_\odot$ (S. D. Johnson et al. 2017; K. Tchernyshyov et al. 2022; Y. Zheng et al. 2024), which corresponds to ∼8% of the oxygen budget (S. D. Johnson et al. 2017; Y. Zheng et al. 2024).

Ultimately, these observations and predictions indicate an observable CGM in the halos of dwarf galaxies, much of which is unaccounted for. Further work investigating the CGM-DG's different temperature phases holds promise in mapping the CGM beyond $r \sim 0.5R_{\rm vir}$ and constraining the physical state of the CGM-DG. Modern hydrodynamic simulations can support these goals by providing predictions for ion masses and column densities, the physical conditions of the CGM gas, and halo mass and metal retention.

On the theoretical side, there exists a handful of works studying the state of the CGM-DG within various simulations. In an increased-resolution run of six IllustrisTNG dwarf galaxies, P.-C. Tung & K.-J. Chen (2025) find the majority of CGM gas for $M_{200c} \sim 10^{10.5}$–$10^{11.0} M_\odot$ galaxies exists at temperatures between $10^3 < T < 10^4$ K which spans a range of densities. This differs from the Auriga simulations for the same halo masses, where the median mass-weighted temperature of CGM gas lies within $10^{4.5} < T < 10^5$ K (A. W. S. Cook et al. 2025). Dwarf galaxy studies from FIRE, like those of IllustrisTNG, find that the CGM-DG roughly follows pressure equilibrium (for FIRE, see Figure 11 of F. Li et al. 2021; for IllustrisTNG, see Figure 3 of P.-C. Tung & K.-J. Chen 2025).

In terms of metal content, simulations appear to show that dwarf galaxies are more efficient at ejecting metals from their disk than Milky Way–mass galaxies (e.g., C. R. Christensen et al. 2016; A. L. Muratov et al. 2017; Z. Hafen et al. 2019; M. Mina et al. 2021). However, different simulations do not necessarily agree on the fraction of metals retained within the halo and CGM of dwarf galaxies. FIRE (Z. Hafen et al. 2019) finds that dwarf galaxies can retain between 30%–100% of their metals within all gas inside R_{200c} and 10%–60% in their CGM, while C. R. Christensen et al. (2018) finds lower retention when considering all gas within R_{200c} (30%–60%) and CGM (15%–25%). These differences likely arise from different feedback modeling; however, although both studies span a wide galaxy mass range, they ultimately utilize a relatively small sample of galaxies in the dwarf galaxy regime.

Ultimately, the baryon cycle of dwarf galaxies, the state and metal content of the CGM-DG, the relationship between the CGM-DG and the evolution of the dwarf galaxy, and the bulk properties of the galaxy and halo remain open questions. Furthermore, current theoretical literature investigating these questions is limited by small sample sizes of individual galaxies, so that the galaxy–galaxy scatter in CGM-DG properties remains underconstrained. We address these issues and questions in this work by using a larger sample of isolated, high-resolution, fully cosmological dwarf galaxies to study the metal content and physical structure of the CGM-DG and provide theoretical predictions and estimates for future observations studying the low-mass CGM.

The paper is organized as follows. Section 2 includes details on the simulation suites we use in this work. Section 3.1 compares our galaxies with observed scaling relations, while Section 3.2 describes the synthetic column densities' generation and agreement with CGM observations. Section 4 presents mass and metal retention rates of the halo ($r < R_{200c}$) and CGM ($0.15R_{200c} < r < R_{200c}$). Section 5 details the physical properties (density, temperature, metallicity) and ionization fractions of the CGM and the total mass accessible via UV observations. Section 6 discusses the implications of our results for CGM-DG observations, how this work relates to previous work, and its limitations. We conclude and summarize in Section 7. In Appendix A, Table 3, we provide individual simulated galaxy properties.

2. Simulations

This work uses two suites of simulations, the Marvel-ous Dwarfs and the Marvelous Massive Dwarfs. These are cosmological zoom-in simulations (e.g., J. Onorbe et al. 2013) and are run with the *N*-body, smoothed-particle hydrodynamics code ChaNGa (H. Menon et al. 2015). Both suites track the evolution of hydrogen, helium, oxygen, iron, and total metallicity. These simulations and the subgrid physics implemented have been shown to reproduce observed scaling relations for stellar-halo mass, metallicity, luminosity, gas content, and size, and produce galaxies with dark matter cores (F. Munshi et al. 2021; B. Azartash-Namin et al. 2024; D. Ruan et al. 2025). Given their well-tested success, these state-of-the-art simulations are the ideal tools for this study. The subgrid physics that is common between suites is summarized below. The differing specifications of the two suites are discussed in Sections 2.1 and 2.2, and the final sample selection and pertinent definitions are presented in Section 2.3.

Metal-line cooling is implemented using cooling and heating rates calculated before runtime (S. Shen et al. 2010). These rates are determined using the nebular photoionization code CLOUDY and assume the redshift-dependent UV photoionizing background provided in F. Haardt & P. Madau (2012). This UV background is chosen to match the same applied during runtime when modeling photoionization.[11] Cooling and heating rates are interpolated during runtime

[11] See A. Obreja et al. (2019) and E. Taira et al. (2025) for discussions of how the choice of UV background impacts the CGM.

based on the density, temperature, metallicity, and redshift. In addition to metal cooling that follows CLOUDY tables, the total radiative cooling in our simulations also incorporates cooling/heating from Compton processes and cooling from primordial species (H I, H_2, H II, He I, He II, and He III). Additionally, both suites include prescriptions for dust, H_2 self-shielding, and dust shielding of H I.

Star formation is only permitted in gas particles that are sufficiently cold ($T < 1000$ K) and dense ($n > 0.1\, m_{\rm H}\,{\rm cm}^{-3}$) (C. Christensen et al. 2012). Once these criteria are met, star formation then occurs probabilistically. Equation (1) describes the probability, p, of gas particles forming stars in a time step Δt:

$$p = \frac{m_{\rm gas}}{m_{\rm star}}\left(1 - \exp\left[\frac{-c_0^* X_{\rm H_2}\Delta t}{t_{\rm form}}\right]\right), \quad (1)$$

where $m_{\rm gas}$ and $m_{\rm star}$ are the particle gas mass and initial mass of the potential star particle, respectively. c_0^* is the star formation efficiency parameter, for which we adopt a value of $c_0^* = 0.1$. $X_{\rm H_2}$ is the fraction of molecular hydrogen. Finally, $t_{\rm form}$ is the local free-fall time. Once star formation has been triggered, a star particle is created with an initial stellar mass distribution according to the P. Kroupa (2001) initial mass function. We note that, despite the density threshold for star formation being relatively low/diffuse, star formation usually occurs only in gas particles of $n > 100\, m_{\rm H}\,{\rm cm}^{-3}$, due to the dependence on $X_{\rm H_2}$.

When a SN event occurs, thermal energy, mass, and metals are deposited into the surrounding environment. The subsequent evolution of the SN remnant is modeled differently by the two suites, and both implement different total values for the injected thermal energy (see Sections 2.1 and 2.2, for more details). Despite this, we note that throughout this work, we do not find strong differences between these suites and their CGM properties. We include figures in Appendix B explicitly showing a comparison of the column densities between the two suites, and differentiate the simulations in plots in the main text where feasible.

Across both suites, all Type Ia SN (SN Ia) events eject $1.4\, M_\odot$ of mass, including $0.63\, M_\odot$ of iron and $0.13\, M_\odot$ of oxygen (following yields presented in F. K. Thielemann et al. 1986), which is deposited into the surrounding gas particles. Stellar winds are also identically modeled in both suites. Mass and metal return via winds is modeled for stars within the stellar mass range of 1–8 $M_\odot$. The fraction of mass returned to the interstellar medium (ISM) takes the functional form presented in V. Weidemann (1987) and is then imparted, along with its fractional metal content, to gas particles in the vicinity of the star particle. The scheme for metal diffusion, which drives the distribution of metals after SN-driven outflows, is also presented in S. Shen et al. (2010).

Black hole (BH) formation and feedback are largely common between the two suites, but the numerical values of certain parameters differ and are provided in the following subsections. Generally, BHs are allowed to form from gas particles that must have low metallicity, high density, cool temperature, and low molecular gas content. Additionally, the gas particle must exceed the Jeans mass criterion. These requirements restrict BH formation to gas that would collapse quickly and cool slowly (R. S. Sharma et al. 2020; J. M. Bellovary et al. 2021). The initial mass of the BH differs slightly between suites and is summarized below. Upon formation, the BH particle accretes mass from surrounding gas particles until it depletes the neighboring mass within one softening length or reaches the seed mass. During accretion, thermal feedback from the BH is injected into the nearest-neighbor particles at a rate equal to the mass-accretion rate. The thermal evolution of the feedback-heated gas particles then follows the SN feedback prescription. The BH model has been found to reproduce galaxies that align with the central supermassive black hole mass–bulge stellar dispersion ($M_{\rm BH}$–σ), stellar mass–halo mass (M_*–$M_{\rm halo}$), and mass–metallicity scaling relations (M. Tremmel et al. 2017). However, initial results that included the Marvel-ous Dwarfs simulations showed that BHs in dwarfs grow little over a Hubble time and do not strongly impact the evolution of the dwarfs (J. M. Bellovary et al. 2021). The BH evolution in the Marvelous Massive Dwarfs will be studied in future work, but we assume there is little impact on the CGM from the BH prescription, similar to the Marvel-ous Dwarfs.

2.1. Marvel-ous Dwarfs

The Marvel-ous Dwarfs (Marvel hereafter) simulations are cosmological zoom-in simulations presented in F. Munshi et al. (2021) and utilized in J. M. Bellovary et al. (2021), C. R. Christensen et al. (2024), B. Azartash-Namin et al. (2024), and C. L. Riggs et al. (2024). In total, there are four 25^3 Mpc^3 regions ("cptmarvel," "rogue," "storm," and "elektra") encompassed by the Marvel suite, which were simulated with WMAP3 cosmology (D. N. Spergel et al. 2007). These simulations are run by choosing a region of the universe that contains several dwarf galaxies and rerunning this zoomed-in region with higher resolution. For each region, the most massive galaxies are $M_* \sim 10^{9.3}\, M_\odot$, while the smallest galaxies are $M_* \sim 3000\, M_\odot$ ultra-faint dwarf galaxies. All galaxies are 1.5–7 Mpc away from a Milky Way–mass galaxy (C. R. Christensen et al. 2024). Marvel has a force resolution of 60 pc, gas particle mass resolution of 1410 $M_\odot$, initial star particle mass resolution of 420 $M_\odot$, and dark matter particle mass resolution of 6650 $M_\odot$.

Stellar feedback from Type II SNe (SNe II) follows the "blastwave" (BW) SN feedback model (G. Stinson et al. 2006). Only massive stars of 8–40 $M_\odot$ produce SNe II. When this occurs, thermal energy ($E_{\rm BW} = 1.5 \times 10^{51}$ erg) is deposited into the gas particles within the radius of a SNe BW according to R. A. Chevalier (1974), as modeled by Equation (9) in G. Stinson et al. (2006). In addition to thermal energy, mass and metals (oxygen and iron) are also deposited, with total mass values according to yields derived in C. M. Raiteri et al. (1996). After the initial thermal dump, the adiabatic or Sedov phase then begins, which is the period where the BW expands but is not able to cool efficiently due to long cooling timescales. To simulate this inefficiency of cooling and prevent numerical overcooling, the BW model disables cooling in the SNe-heated gas particles during the Sedov phase. Subsequently, the BW enters the snowplow phase, where momentum is conserved and cooling is reenabled.

BH formation proceeds in gas particles that satisfy the following conditions: low metallicity ($\log Z < -4$), high density ($1.5 \times 10^4\,{\rm cm}^{-3}$), low temperature ($T < 2 \times 10^4$ K), and low molecular gas content ($f_{\rm H_2} < 10^{-4}$). The resulting BH has an initial mass of $5 \times 10^4\, M_\odot$, and BH feedback follows the BW SN feedback model.

2.2. Marvelous Massive Dwarfs

The Marvelous Massive Dwarfs are cosmological zoom-in simulations of dwarfs selected from the Romulus25 cosmological volume simulation (M. Tremmel et al. 2017) and utilized in B. Keith et al. (2025) and D. Ruan et al. (2025). The Massive Dwarfs are run within a Planck cosmology (Planck Collaboration et al. 2016), and initial conditions were generated using GenetIC (S. Stopyra et al. 2021). The simulations have a force resolution of 87 pc, gas particle mass resolution of 3300 $M_\odot$, initial star particle mass resolution of 994 $M_\odot$, and dark matter particle mass resolution of 17,900 $M_\odot$.

Stellar feedback follows the "superbubble" (SB) SN feedback model (B. W. Keller et al. 2014). This model is motivated by the spatial and temporal clustering of star formation and, consequently, stellar feedback, which leads to SBs of feedback rather than isolated events. The SB model is similar to the BW model in that it deposits thermal energy ($E_{\rm SB} = 1.0 \times 10^{51}$ erg) and the same total mass and metals into the surrounding medium. However, the SB model deposits this energy into one neighboring gas particle, and the SNe energy then diffuses into the surrounding gas particles according to thermal conduction and evaporation subgrid models (L. L. Cowie & C. F. McKee 1977; B. W. Keller et al. 2014). To prevent numerical overcooling, SB models SNe-heated particles as multiphase fluid elements, or "two-phase particles," if the mass of the particles is not fully heated. These two-phase particles model two temperature phases, a hot and a cold phase, which remain in pressure equilibrium with one another and have individual masses, densities, and temperatures. This method aims to simulate the SNe-heated gas (hot phase) that sweeps up ISM material (cold phase) seen in SBs. Mass exchange from the cold to the hot phases is calculated via the subgrid thermal evaporation model. Once the cold mass has been fully evaporated, or if the hot phase cools below 10^5 K, the two-phase particle returns to the single-phase state. For the analysis in this work, we average the temperature and density of any two-phase particles to treat them as single-phase particles. We find these two-phase particles account for ∼5% of the CGM by mass and ∼10% of the CGM by metal mass, yet these particles tend to have little effect on column densities and temperature budgets.

BH formation proceeds in gas particles that satisfy the following conditions: low metallicity ($\log Z < -5$), high density ($1.5 \times 10^4\,{\rm cm}^{-3}$), cool temperature ($T < 5 \times 10^3$ K), and low molecular gas content ($f_{\rm H_2} < 2 \times 10^{-3}$). The resulting BH has an initial mass of $1.2 \times 10^5\,M_\odot$, and BH feedback follows the SB feedback model.

2.3. The M + M Sample

Using the Marvel and Marvelous Massive Dwarfs simulations, star-forming (specific star formation rates, sSFRs $\geqslant 10^{-11}$ in the 100 Myr prior to $z = 0$) dwarf galaxies were selected to match the stellar mass range of $6.0 \leqslant \log(M_*/M_\odot) \leqslant 9.5$ used in Y. Zheng et al. (2024). The $z = 0$ snapshots are used to correspond to the low-redshift sample presented in Y. Zheng et al. (2024). Additionally, only dwarf galaxies that are at least 200 kpc away from the center of mass of a $M_* > 10^6\,M_\odot$ galaxy were chosen to avoid contamination from other halos in synthetic column densities and global CGM properties. With these criteria, 24 dwarf galaxies were selected from the Marvel suite, and 40 dwarf galaxies were selected from the Marvelous Massive Dwarfs suite to comprise the Marvel+Marvelous Massive Dwarfs ("M + M") sample.

A summary of stellar mass (M_*), virial radius (R_{200c}), virial mass ($M_{\rm vir}$), and total halo gas mass ($M_{\rm gas}$) is shown in the top panel of Figure 1, and a comparison of stellar masses between the M + M sample and Y. Zheng et al. (2024) sample is shown in the bottom panel. A sample of $z < 0.3$ galaxies observed in N. Mishra et al. (2024) is also included and used for comparison throughout this work. We find adequate agreement between the stellar mass distributions of the full simulated sample and the total observed sample. In this work, the virial radius of a galaxy is taken as the radius within which the average density is 200 times the critical density of the Universe (R_{200c}), which is lower by a factor of 0.6 than the matter density definition (R_{200m}).

In the M + M sample, we define the CGM as all material within $(0.15–1)R_{200c}$. This boundary was chosen to select particles residing in the extended CGM and remove those within the disk of the galaxy. This method of defining the CGM as a fixed fraction of the virial radius is similar to many other studies in the field (e.g., Z. Hafen et al. 2019; F. Li et al. 2021; A. W. S. Cook et al. 2025). We note, however, that with decreasing halo mass, the size of the disk relative to the halo shrinks. Consequently, at the low-mass end, we exclude mass that an observer would likely consider the CGM. We opt to adopt a standardized definition across masses for simplicity and clarity, but discuss the repercussions of this in Appendix C.

3. Comparison to Observations

In this section, we verify that our galaxies match key empirical scaling relations, as well as observed CGM column densities, before using them to interpret the CGM of observed dwarf galaxies.

3.1. Galaxy Observables

Scaling relations between physical properties of galaxies have been used to empirically describe galaxy evolution (e.g., K. B. W. McQuinn et al. 2020; Y.-H. Lin et al. 2023). For example, the luminosity–metallicity relation provides insight into the chemical evolution of a galaxy since the present-day metal content of a galaxy arises from the combined effects of star formation, feedback-driven metal loss, and accretion of pristine gas (J. J. Dalcanton 2007; K. B. W. McQuinn et al. 2020).

The left panel of Figure 2 shows the mean luminosity–metallicity relation for the M + M sample (red and blue markers) compared to Local Group dwarf galaxy observations (open gray circles; A. W. McConnachie 2012) and the Local Volume Database (open gray diamonds; A. B. Pace 2025).[12] For each simulated galaxy, we represent the 16th–84th percentile range of the stellar metallicities as error bars, and plot the median values of both suites as solid lines. We find the stellar metallicities of the M + M sample reproduce the majority of observations within the simulated error bars. Further, we observe no systematic difference between suites, despite limited observations on the higher-mass dwarf end. The agreement between simulations and observations confirms that realistic masses of metals are retained within the stellar populations.

[12] In the case of duplicate measurements between A. W. McConnachie (2012) and A. B. Pace (2025), we choose to show the measurements from A. W. McConnachie (2012).

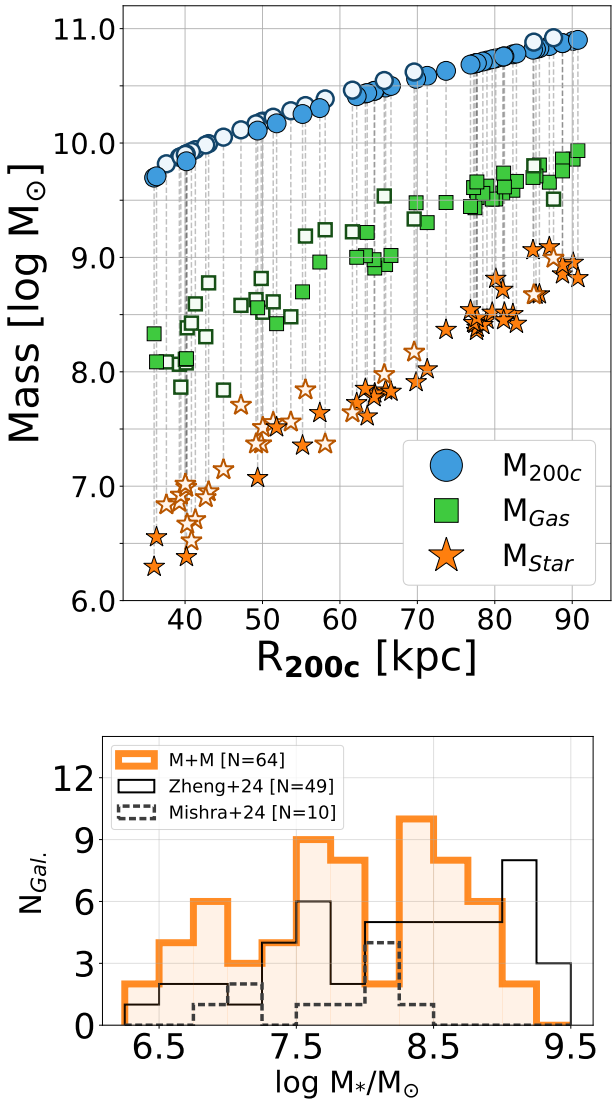

Figure 1. Top panel: summary of the virial mass (blue circle), total gas mass in the halo (green square), and stellar mass (yellow star) for each galaxy in the Marvel simulation (open-faced markers) and the Marvelous Massive Dwarfs simulations (filled markers). The galaxies in the Marvelous Massive Dwarfs have slightly greater virial masses for a given virial radius than the Marvel galaxies due to the difference in cosmology (see Section 2). Bottom panel: histograms of stellar masses for the observed galaxies (Y. Zheng et al. 2024, solid black line; N. Mishra et al. 2024, dashed gray line) and histogram of stellar masses for the M+M sample (orange). All simulated stellar masses are 0.6 of the total sum of star particle masses within a halo, as this is a better match to photometric stellar mass determinations (F. Munshi et al. 2013). All galaxies included in Y. Zheng et al. (2024) and the $z < 0.3$ galaxies included in N. Mishra et al. (2024) are shown in this plot. These values are also provided in Table 3 for each galaxy in the M+M sample.

The galaxy sSFR–stellar mass relation (e.g., T. K. Wyder et al. 2007) provides observational constraints on sSFRs for a given galaxy stellar mass (M_*). The right panel of Figure 2 presents sSFR values for the M+M sample and observations (open-faced markers). We find a substantial degree of scatter (∼1.5 dex) for $\log(M_*/M_\odot) < 8.0$ in the simulations, which agrees with the scatter in observations in this mass range. While there is a similar degree of scatter for $\log(M_*/M_\odot) > 8.0$, the simulations tend to produce galaxies biased toward greater sSFR. However, across stellar masses, the M+M sample exhibits sSFRs that agree with observational values. Across suites, we find both produce galaxy populations ranging in similar values of sSFR. We also note that the bias toward greater sSFR for $\log(M_*/M_\odot) > 8.0$ appears to be present in both suites. Given the agreement between simulations and observations in Figure 2, we find that the M+M sample contains galaxies with realistic star formation rates for their stellar masses.

The agreement shown in Figure 2 indicates our simulations produce galaxies with realistic star formation rates and metal contents, thereby motivating the choice to use these simulations to study the CGM-DG.

3.2. CGM Observables—Column Densities

Figure 3 shows projected column density maps in H I, Si II, C IV, and O VI of a representative galaxy in the M+M sample (a $\log M_*/M_\odot = 8.82$ galaxy from the Marvelous Massive suite). We find H I, Si II, and C IV column densities are greatest closest to the galaxy and decrease with increasing distance from the galaxy. Si II columns tend to be largest only in the inner CGM and very low in the outer CGM. H I columns are also largest in the inner CGM; however, in the outer regions H I tends to have a uniform $N_{\rm HI} \sim 10^{14}$ cm^{-2} coverage. O VI column densities tend not to vary strongly with distance from the galaxy. Furthermore, we find that column densities in species of low ionization potential (H I and Si II) tend to trace denser and cooler structures in the inner CGM, while species of intermediate and high ionization potential (C IV and O VI) exhibit column densities that trace a volume-filling medium. This qualitative behavior is generally in agreement with other simulations (e.g., A. W. S. Cook et al. 2025).

Column densities for the M+M sample were calculated by generating 325 lines of sight around each galaxy. Each sightline is 0.25 Mpc in length to avoid intersecting another galaxy's CGM while still probing the surrounding environment of the dwarf galaxy. Additionally, each sightline is randomly oriented with respect to the disk and centered at a random impact parameter, b, from the disk. This methodology allows us to randomly sample each galaxy in the M+M sample at a range of projected distances and inclination angles. To fully sample the CGM and avoid intersecting the disk of the galaxy, the sightlines are generated within $b/R_{200c} = [0.15, 1.3]$. The physical length scales for the virial radii in the M+M sample are shown in Figure 1.

Sightline positions and path length elements are generated using TRIDENT (C. B. Hummels et al. 2017), which relies on the simulation analysis `yt` (M. J. Turk et al. 2011). As aforementioned, the M+M sample simulations track hydrogen, oxygen, and iron throughout the runtime by tracking the mass fraction of each element for each gas particle (the same method as used in M. Mina et al. 2021). The abundances of other elements are added in during the analysis phase by using the relative abundances of a tracked element and a nontracked element from M. Asplund et al. (2009; i.e., $f_C = f_O \times (A_C/A_O)$). Ion fractions for each element are generated using CLOUDY (G. J. Ferland et al. 2017) and added to each particle in the simulation during postprocessing based on the particle's density, temperature,[13] and redshift. The same redshift-

[13] CHANGA converts particle internal energy into temperature via the ideal gas law. The mean molecular weight is computed from nonequilibrium abundances of H I and H II, and He I, He II, and He III, with metals contributing an additional term that scales with metallicity ($\mu_Z = 17.6003$). Metal cooling is also tabulated; see further details in S. Shen et al. (2010) and Section 2.

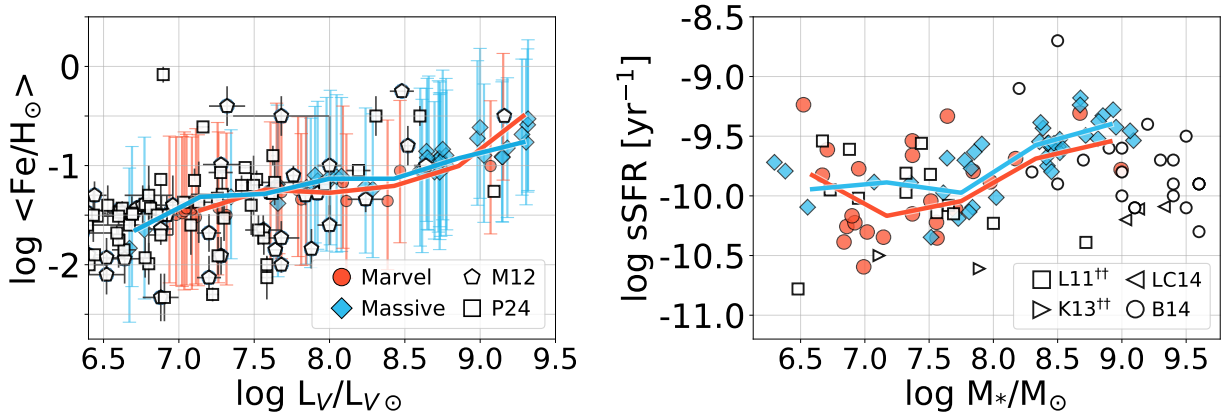

Figure 2. Luminosity–metallicity relation (Fe/H vs. L_V; left) and galaxy specific star formation rates (sSFR vs. M_*; right). Red circles represent galaxies from the Marvel suite, and blue diamond markers represent the Marvelous Massive suite; median values of both suites are shown as solid lines. Left panel: shown is the logarithm of the mean stellar metallicity relative to solar abundance. Error bars on simulated points show the 16th–84th percentile range of the simulated stellar metallicity distribution. Open-faced pentagon markers are observational data from A. W. McConnachie (2012), and open-faced square markers are observational data from the Local Volume Database (A. B. Pace 2025). Right panel: sSFR values for the M+M sample are calculated over a timescale of 100 Myr (sSFR values for individual galaxies are provided in Table 3). Open-faced markers are observations that derive star formation rates as follows: R. Bordoloi et al. (2014) use detected nebular emission lines, and C. J. Liang & H.-W. Chen (2014) use rest-frame UV absolute magnitude. I. D. Karachentsev et al. (2013) and J. C. Lee et al. (2011) values utilize far-UV magnitudes and are corrected for Galactic extinction in Y. Zheng et al. (2024) following the methods presented in their Appendix. We find adequate agreement between the M+M sample and observations, as well as similar behavior across suites.

dependent photoionizing UV background from F. Haardt & P. Madau (2012) that is implemented in the simulations is used to generate ion fractions as well. We assume that the ionizing radiation from the central galaxy is negligible based on the low star formation rates seen in the M+M sample (Figure 2); however, see Section 6.4 for a discussion on how this may affect our results. Column densities are then calculated by summing the product of the ion number density and the path length element across the line of sight.

To compare to observations, we present results for the ions H I, C II, C IV, Si III, Si IV, and O VI. We choose to omit Si II in this section, as it shows similar trends to C II; however, we include it in Appendix B (along with figures showing the column density results differentiated by simulation suite).

Figure 4 shows the simulated column densities for H I, C II, and Si III as a function of normalized impact parameter, b/R_{200c}. Each figure column shows 2D probability histograms for all simulated galaxies within a given stellar mass bin (denoted at the top of each column), and each row shows the results for a given ion. The solid black line represents the median column density for the M+M sample. Observational data from Y. Zheng et al. (2024) and a subsample of N. Mishra et al. (2024; described in Section 2) are shown as points on each figure. Black points represent detections in a given ion, while white points with a downward-pointing arrow are nondetections and are treated as upper limits. Black points with an upward-pointing arrow are saturations and are treated as lower limits. Black bars are intervals provided in N. Mishra et al. (2024) that show the upper and lower limits for saturated systems. The marker style of each point signifies the publication of the observation (legend located at the bottom of the figure), and the key follows the same style as Figure 4 from Y. Zheng et al. (2024) for comparison sake.[14] Table 1 quantifies the agreement with observations by presenting the number of detections encompassed by 1 and 2 standard deviations (σ) from the total M+M sample median (black lines in Figures 4 and 5).

H I column densities. We find broad agreement between the M+M sample and observations of H I column densities ($N_{\rm HI}$). For log $(M_*/M_\odot) > 7.5$ galaxies, the synthetic $N_{\rm HI}$ distributions encompass 70% (10/14) of observations within 2σ. For galaxies with log $(M_*/M_\odot) < 7.5$, the M+M sample reproduces all observations (2/2) within 2σ, although only two detections are available. Further, there are no $N_{\rm HI}$ observations of the inner CGM of $6.0 <$ log $(M_*/M_\odot) \leqslant 7.5$ galaxies that meet our selection criteria.

$N_{\rm HI}$ values fall off steeply in the inner CGM $b/R_{200c} < 0.5$, a feature also seen in Figure 3. Currently, only observations of log $(M_*/M_\odot) > 7.5$ galaxies probe this inner region of the CGM, and there is a mixture of detections and lower limits. Simulated galaxies of the same mass exhibit inner $N_{\rm HI}$ profiles generally above these observations, which agrees with the published lower limits while having the detections on the edge of the distribution. We find that with decreasing galaxy mass, the inner $N_{\rm HI}$ profile becomes less steep, a feature discussed further in Section 6. For $b/R_{200c} > 0.5$, the $N_{\rm HI}$ profiles become much flatter and plateau at $N_{\rm HI} \sim 10^{14.0}$ cm^{-2} (see also M. Mina et al. 2021; A. W. S. Cook et al. 2025) and Figure 3. Interestingly, the $N_{\rm HI}$ value that the profiles plateau to shows little dependence on host galaxy mass; a physical interpretation for this is also provided in Section 6.

Low metal ion column densities. We find that all metal ion column densities fall off with increasing impact parameter, and median values decrease with decreasing host stellar mass. Low ions (C II, Si II, Si III) fall off steeply (also seen in Figure 3), dropping below detectable limits by $0.5R_{200c}$. Within this inner CGM, the M+M sample reproduces 2/4 existing C II detections and 7/8 Si III detections within 2σ. Beyond $0.5R_{200c}$, these low ions have fallen well below detectable limits and match the published upper limits. Thus, the M+M sample shows similar trends to observations, and the majority of detections are within 2σ.

[14] Key differences between Figures 4 and 5 and Figure 4 of Y. Zheng et al. (2024): Y. Zheng et al. (2024) utilizes the virial definition of 200 times the matter density of the Universe. As we use 200 times the critical density of the Universe, we have shifted the observed points to $b/R_{\mathbf{200c}}$ and sorted the observations by stellar mass.

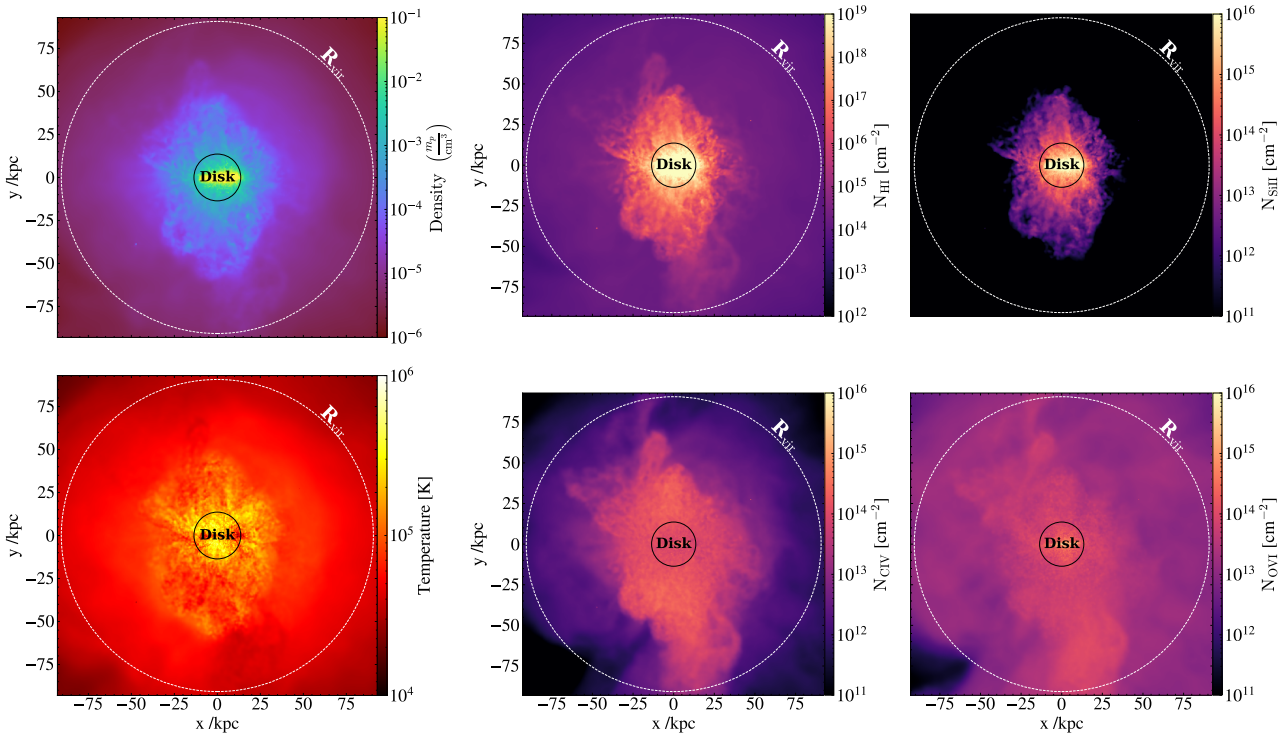

Figure 3. Projected maps of CGM gas density (upper left), gas temperature (lower left), H I column density (upper center), Si II column density (upper right), C IV column density (lower center), and O VI column density (lower right) using TRIDENT (C. B. Hummels et al. 2017) and `yt` (M. J. Turk et al. 2011). Maps are made for a typical galaxy in the M + M sample (a $\log M_*/M_\odot = 8.82$ galaxy from the Marvelous Massive suite). In each panel, we show the R_{200c} as the dashed white line and $0.15R_{200c}$ as the solid black line. The galaxy disk is oriented in the panel such that the disk is edge-on.

Intermediate metal ion column densities. Figure 5 is the same as Figure 4 but for ions of higher ionization potential: Si IV, C IV, and O VI. For these ions, column densities decrease with increasing impact parameters. This decline in column density is shallower than the low ions while also falling below detection limits by $0.5R_{200c}$, agreeing with published upper limits. Within $0.5R_{200c}$, Si IV column densities show broad agreement with observations, with $3/4$ of detections within 2σ. However, C IV column densities show weaker agreement with observations. With existing detections, $5/8$ detections lie within 2σ and $0/8$ detections lie within 1σ. This likely indicates the M + M sample underpredicts C IV, and we present a brief analysis on what may be driving this lack of C IV in Section 6.1.

High metal ion column densities. Column densities for O VI (N_{OVI}) are provided in Figure 5 and are compared with observations from S. D. Johnson et al. (2017) and N. Mishra et al. (2024). No observations from Y. Zheng et al. (2024) are shown because the O VI $\lambda\lambda$1032, 1038ÅÅ transition is not observable at $z \sim 0$. Thus, we note that the N_{OVI} observations shown do have a median redshift of $z \sim 0.15$ and are, therefore, at systematically higher redshifts than the M + M sample. Despite this difference in redshift, we find the M + M sample produces N_{OVI} values below all observed detections by $\sim$1–1.5 dex and near the observational threshold of $N \sim 10^{13}\,\mathrm{cm}^{-2}$. Further, the M + M sample reproduces $0/6$ observations within 2σ. Thus, the M + M sample underestimates N_{OVI} compared to observations. A brief investigation into O VI at higher redshifts and an interpretation for this underprediction are provided in Section 6.1.

Column density scatter. At a given impact parameter, the distributions shown in Figures 4 and 5 can range >1 dex in column densities. Given the number of galaxies in the M + M sample, we can quantify the scatter in column densities for a single CGM and the galaxy–galaxy scatter to assess which is driving this range. For N_{HI}, N_{CIV}, and N_{OVI}, the difference between the 16th and 84th percentiles in a bin size of $0.02\,b/R_{200c}$ is on the order of 0.5 dex, while the spread in N_{CII}, N_{SiII}, N_{SiIII}, and N_{SiIV} tends to be larger with typical values between 0.6 and 1 dex. While this scatter is nonnegligible, we see a greater spread when considering galaxy–galaxy scatter. In particular, median column density profiles for individual galaxies tend to range from 0.5 to 2 dex. These findings can be seen in Appendix B (Figures 13 and 14), where we provide the median column density profiles and their 16th and 84th percentiles for each galaxy in the M + M sample. Ultimately, including a large number of galaxies in the M+M sample has a greater effect on the scatter in column densities; however, the spread in column densities within a single CGM also increases this scatter.

4. CGM Budget

Motivated by the agreement in most ions between existing observations and the M + M sample, the following sections aim to contextualize the column densities and their profiles based on the properties of the CGM. The lack of low ion detections seen observationally and small low ion column densities provided in Section 3 likely indicate either (a) dwarf galaxies do not effectively retain metals/mass in the outer CGM, or (b) there is a prominent warmer phase where ion fractions for low ions are small. To differentiate between these possibilities, the following sections present the halo mass retention (Section 4.1) and metal retention (Section 4.2). In Section 4.3, we assess how the mass and metal retention rates vary by CGM gas phase.

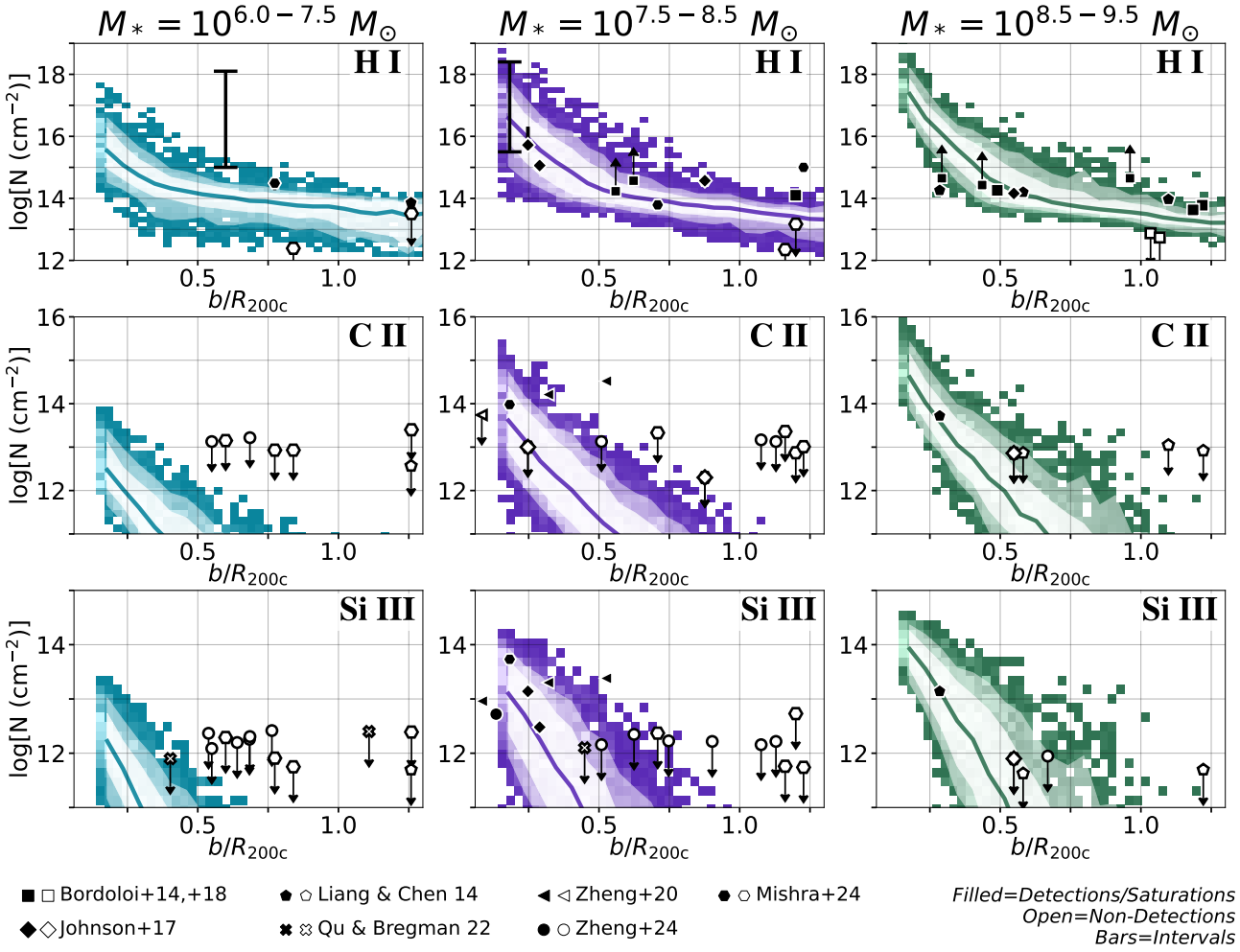

Figure 4. Adapted Figure 4 from Y. Zheng et al. (2024) showing column densities (N) for low ions (H I, C II, and Si III) as a function of normalized impact parameter (b/R_{200c}). The column density results from the M+M sample are shown as 2D probability density histograms with the brightest cells showing a greater probability at a given b/R_{200c}. The median of all simulated columns as a function of b/R_{200c} is shown as a solid line with two shaded regions representing the 16th–84th (1σ) and 5th–95th percentiles (2σ). Observed column densities are shown as points, where each marker is attributed to a certain observational paper (legend shown at the bottom of the figure). Open markers are nondetections and are treated as upper limits, while filled markers are detections; filled markers with upward arrows are saturations and are treated as lower limits. Black bars are intervals provided in N. Mishra et al. (2024) that show the observationally constrained range (upper and lower limits) of column densities for saturated systems. Each column shows all simulated and observational data for the CGM around galaxies within a given stellar mass bin (denoted at the top). From left to right, the three stellar mass bins (and the number of simulated galaxies in each bin) are as follows: $M_* = 10^{6.0-7.5}\ M_\odot$ ($N = 19$), $M_* = 10^{7.5-8.5}\ M_\odot$ ($N = 29$), and $M_* = 10^{8.5-9.5}\ M_\odot$ ($N = 16$). We find the M+M sample reproduces the majority of existing column density observations for the low ions included in this work (see also Table 1).

4.1. Mass Budget

The halo mass retention can be described by the contributions of all baryons to the baryonic budget. The baryonic budget provides insight into the fraction of baryons present in a given halo with respect to the "expected" or cosmological abundance of baryons. The cosmological baryonic budget ($f_{b,\mathrm{Cosmo}}$) is defined as

$$f_{b,\mathrm{Cosmo}} = \frac{m}{M_{\mathrm{vir}} \cdot \Omega_b/\Omega_M}, \quad (2)$$

where the denominator represents the "expected" abundance of baryons for a given halo mass based on the cosmological baryon (Ω_b) and matter density (Ω_M). The numerator (m) represents any mass of interest (e.g., CGM mass, ISM mass, etc.). Deviations from a baryonic budget of unity suggest mass loss from the halo via feedback (e.g., R. Davé 2009).

The upper panel of Figure 6 shows $f_{b,\mathrm{Cosmo}}$ for each galaxy in the M+M sample with respect to stellar mass. For a given galaxy, we divide the total baryonic budget into its individual contributions from the stellar component (orange), ISM (dark green), disk–CGM interface (light green), and the CGM (light

Table 1
Summary of the Number of Detections within 1σ and 2σ of the Simulated Distribution Medians Relative to the Total Number of Observed Detections for a Given Ion around a Given Galaxy Mass

	Low M_* $10^{6.0-7.5}\ M_\odot$ 1σ,2σ,(All)	Mid M_* $10^{7.5-8.5}\ M_\odot$ 1σ,2σ,(All)	High M_* $10^{8.5-9.5}\ M_\odot$ 1σ,2σ,(All)
H I	1, 2, (2)	3, 4, (7)	4, 6, (7)
C II	0, 0, (0)	1, 1, (3)	1, 1, (1)
Si III	0, 0, (0)	4, 6, (7)	1, 1, (1)
Si IV	0, 0, (0)	2, 2, (3)	1, 1, (1)
C IV	0, 0, (1)	0, 3, (5)	0, 2, (2)
O VI	0, 0, (1)	0, 0, (5)	0, 0, (0)

Note. Each entry consists of three numbers, and is ordered as detections within 1σ, detections within 2σ, (total number of observed detections).

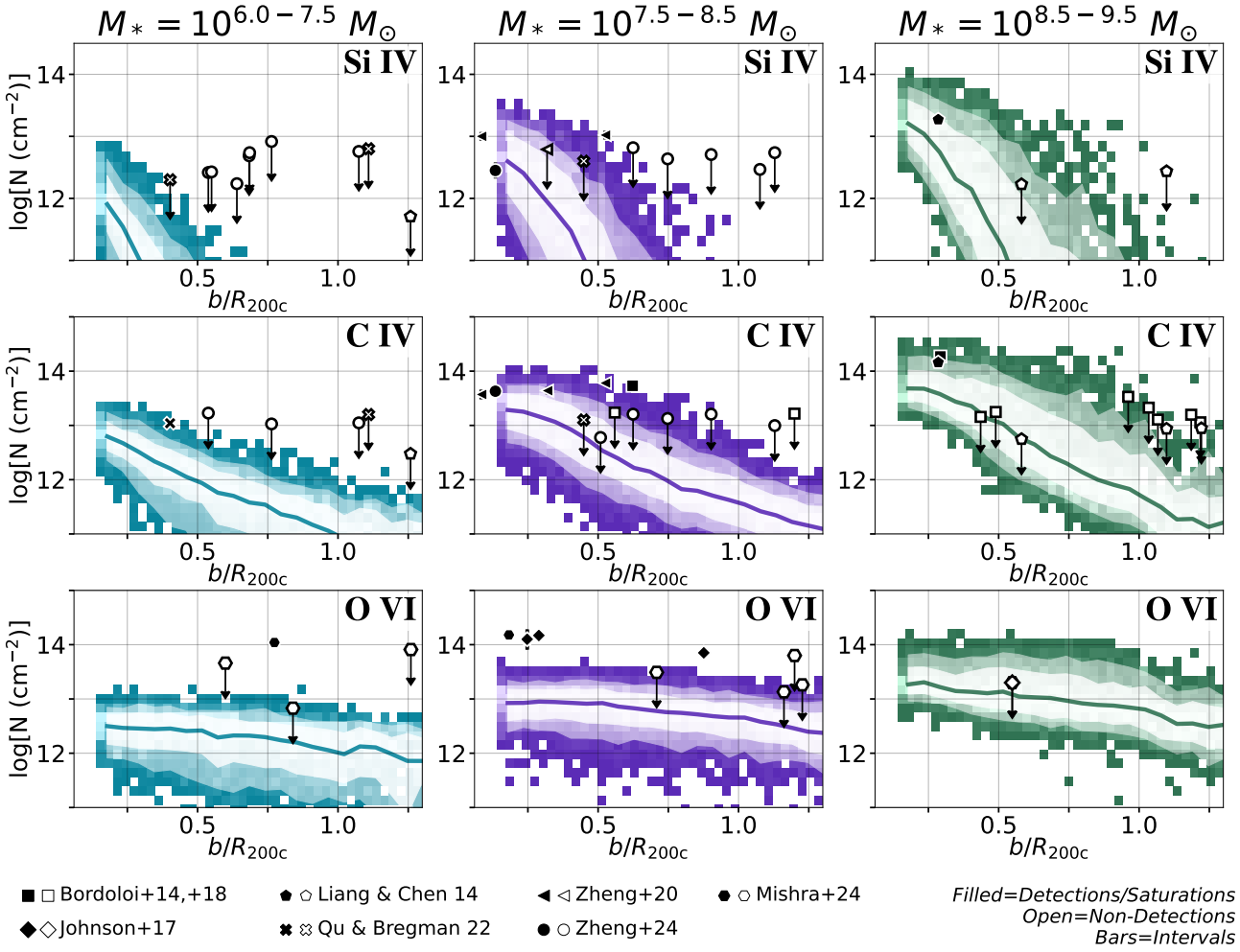

Figure 5. Same as Figure 4 (adapted Figure 4 from Y. Zheng et al. 2024) now showing column densities for higher ions (Si IV, C IV, and O VI). We find the M+M sample reproduces the majority of existing Si IV column density observations, while the simulations tend to underpredict C IV and O VI column densities (see Section 6.1 for further discussion).

purple bar). We define the ISM mass as 1.4 times the total H I mass (to determine the total H + He mass) within a radius at which the surface density of H I (as measured when the galaxy is oriented face-on) falls below 1 $M_\odot$ pc^{-2}; hereafter we define this radius as $r_{\Sigma_{\rm HI}}$. This ISM mass definition and surface density limit were chosen to match common observational methods and detection limits of H I surveys (e.g., N. Deg et al. 2024). Once again, we define the CGM as all gas particles within $0.15 < r/R_{200c} < 1$. To fully account for all baryons in the halo, we include the disk–CGM interface, which is the spherical shell between the ISM and CGM, $r_{\Sigma_{\rm HI}} < r < 0.15R_{200c}$.

We find that with declining stellar mass, the total fraction of baryons retained in the halo declines, resulting in dwarf galaxies becoming increasingly dark matter dominated. This decline also indicates an increased sensitivity to feedback with decreasing mass, resulting in more of the dwarf galaxy's baryons being lost from the halo via feedback processes or prevented from accreting onto the halo due to the photoionizing background. The median total baryonic budget and its standard deviation for $\log(M_*/M_\odot) > 8.0$ (28/64 halos in the M+M sample) halos is 0.467 ± 0.050, which falls to 0.183 ± 0.048 for $\log(M_*/M_\odot) < 8.0$ halos. Intuitively, as the total baryonic budget decreases, the contributions from the stars, ISM, and CGM also decline. High-mass dwarf galaxies ($\log(M_*/M_\odot) > 8.0$) in the M+M sample exhibit median CGM contributions of 0.21 ± 0.03, while for low-mass dwarf galaxies ($\log(M_*/M_\odot) < 8.0$) this median drops to 0.09 ± 0.03. In a similar trend, high-mass dwarf galaxies exhibit median ISM and stellar baryonic budgets of 0.14 ± 0.03 and 0.06 ± 0.02, respectively, which fall to 0.03 ± 0.02 and 0.01 ± 0.01 for low-mass dwarf galaxies.

The lower panel of Figure 6 shows the fraction of all baryons within R_{200c} ($f_{b,\rm Halo}$) that reside in the same components (e.g., stars, CGM, etc.) as the upper panel. $f_{b,\rm Halo}$ is defined by the following equation:

$$f_{b,\rm Halo} = \frac{m}{M_{\rm Gas}(<R_{200c}) + M_*(<R_{200c})}, \quad (3)$$

where the denominator is simply the sum of all baryons within the halo in the form of gas ($M_{\rm Gas}$) and stars M_*. Across stellar masses, we find that the CGM of low-mass galaxies tends to contain a comparable, and frequently dominant, fraction of baryons within the halo, as compared to the ISM. For $\log(M_*/M_\odot) > 8.0$, 23/28 galaxies have halo baryonic budgets dominated by the CGM over the ISM. In this mass range, the median $f_{b,\rm Halo}$ values for the CGM and ISM are 0.44 ± 0.07 and 0.30 ± 0.10, respectively. Similarly, 35/36 $\log(M_*/M_\odot) < 8.0$ galaxies have CGM-dominated baryonic

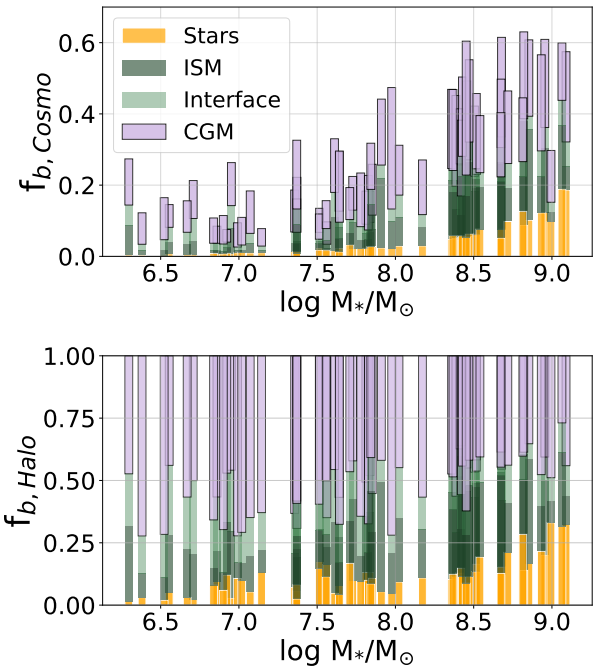

Figure 6. Contributions to the cosmic baryonic budget (top panel, defined as $f_{b,\mathrm{Cosmo}} = M/(\Omega_b/\Omega_m M_{200c})$) and halo baryonic budget (bottom panel, defined as $f_{b,\mathrm{halo}} = M/M_b(< R_{200c})$) from the CGM (uppermost bar, purple) beyond 15% R_{200c}, the disk–CGM interface (light green), the $r_{\Sigma_{\mathrm{HI}}}$-selected ISM (dark green), and stars (bottommost bar, yellow). With decreasing stellar mass, dwarf galaxies show a declining cosmic baryonic budget, yet for all masses the CGM represents a significant (48% ± 11%) reservoir of halo baryons. Individual disk and CGM masses can be found in Table 3.

budgets, with median $f_{b,\mathrm{Halo}}$ values for the CGM and ISM of 0.57 ± 0.10 and 0.16 ± 0.09, respectively. Given these results, the M+M sample predicts there will be a significant portion of baryons in the CGM-DG.

4.2. Metal Budget

In addition to the total baryonic mass, the rate of metals retained in the CGM is pertinent for understanding column densities. We follow the methods presented in N. N. Sanchez et al. (2024) to calculate the metal retention for our galaxies, defined in Equation (4) as

$$f_Z = M_Z/M_{Z,\mathrm{form}}, \tag{4}$$

where M_Z is the total mass in metals present within a given volume (e.g., disk, CGM, halo) and $M_{Z,\mathrm{form}}$ is the total mass of metals formed by the galaxy across cosmic time. To calculate $M_{Z,\mathrm{form}}$, we use PYNBODY (A. Pontzen et al. 2013) to replicate the metal production calculations from SNe Ia and SNe II (done by the simulation during runtime) for all star particles within the galaxy at $z = 0$. That is, we calculate the total mass of metals formed by the galaxy's stars throughout the runtime. The fraction of metals retained (f_Z) is then found by dividing these two masses. This analysis provides insight into how effectively dwarf galaxies eject their metals from their disks and halos.

Figure 7 presents the results for metal retention within the volume of the galaxy (f_Z(Disk Gas+Stars)) versus the CGM (f_Z(CGM)). The disk of a galaxy is defined using $r_{\Sigma_{\mathrm{HI}}}$, the same definition as the baryonic budget analysis. The horizontal axis of Figure 7 shows the metal retention for all disk gas plus

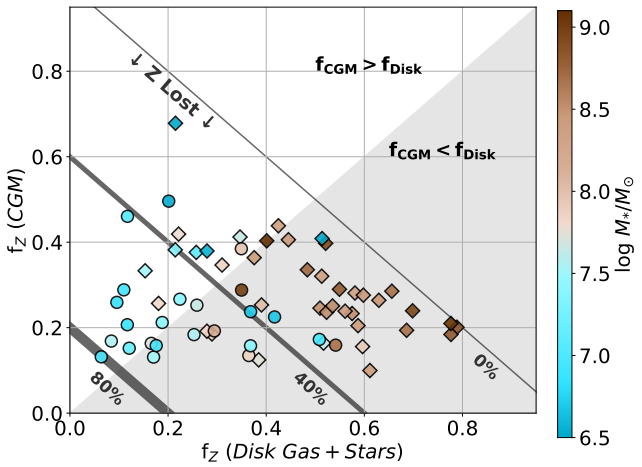

Figure 7. Total halo metal retention for each halo. The horizontal axis shows the fraction of metals retained in the disk (gas and stars), defined by $r_{\Sigma_{\mathrm{HI}}}$. The vertical axis shows the fraction of metals retained in all gas beyond the disk (extended CGM and disk–CGM interface) out to R_{200c}. Galaxies are differentiated by simulation suite by marker type (i.e., Marvel, circles; Massive, diamonds) and color-coded by stellar mass. If a halo lies in the lower-right gray region, then the disk holds more metals than the CGM; the reverse is true in the upper-left white region. The solid gray lines denote the fraction of metals lost relative to the metal mass predicted by the star formation history. For example, if a halo lies on the 40% line, then 40% of the metals are not accounted for and are likely outside of the halo. With decreasing stellar mass, dwarf galaxies are less effective at retaining metals in their disk and more effective at losing metals from their halo; however, the CGM metal retention tends to remain within 0.1–0.45.

the stellar content. The vertical axis shows the value of f_Z for the remainder of the halo out to R_{200c} ($r_{\Sigma_{\mathrm{HI}}} < r < R_{200c}$); this method includes the disk–CGM interface as part of the CGM (see below for the f_Z of the interface region). Each galaxy is shown as a circle or diamond point to differentiate between the Marvel and Massive suites, respectively, and is color-coded by stellar mass. If a given galaxy exists in the gray shaded region in the bottom right of the plot, then the disk of the galaxy holds more metals than the CGM, while if a galaxy exists in the white region in the upper left of the plot, the CGM holds more metals than the disk.

As this method tallies all metals present with R_{200c}, the position of each galaxy also provides an estimate of the fraction of the galaxy's metals that have been lost from the halo ($f_{Z,\mathrm{lost}}$). Each solid line denotes this value, where the thinnest line labeled "0%" denotes that 0% of metals have been lost.

We find that galaxies with higher stellar masses also tend to have more metals within their disk region and have lost $f_{Z,\mathrm{lost}} \sim 10\%$ of their metals from the halo. For log $(M_*/M_\odot) > 8.0$ galaxies, the disk gas contains a median value of $f_{Z,\mathrm{disk}} = 0.47 \pm 0.13$, which exceeds the stellar contribution of $f_{Z,\mathrm{star}} = 0.08 \pm 0.05$. Lower-mass galaxies (log $(M_*/M_\odot) < 8.0$) exhibit smaller retention rates for disk gas, $f_{Z,\mathrm{disk}} = 0.21 \pm 0.13$, and stars, $f_{Z,\mathrm{star}} = 0.02 \pm 0.01$. As stellar mass decreases, the disks of galaxies tend to lose a larger fraction of their metals, and $f_{Z,\mathrm{lost}}$ tends to increase (shift left horizontally). This results in more metals residing in the CGM than the disk of lower-mass galaxies, and these halos losing $f_{Z,\mathrm{lost}} = 40\%$–$80\%$ of metals produced. Interestingly, despite the decrease in $f_{Z,\mathrm{disk}}$ and increase in $f_{Z,\mathrm{lost}}$ with declining stellar mass, the median fraction of metals retained in the CGM tends to remain constant across these stellar masses. The CGM metal retention for the M+M sample remains near 0.25 (log $(M_*/M_\odot) > 8.0$ galaxies, $f_{Z,\mathrm{CGM}} = 0.25 \pm 0.08$; log $(M_*/M_\odot) < 8.0$ galaxies,

$f_{Z,CGM} = 0.23 \pm 0.13$), however with a nonnegligible degree of scatter. In the M+M sample, 60/64 (94%) of galaxies exhibit CGM retention rates between 0.1–0.45.

Disk–CGM interface retention. The fraction of metals retained in the disk–CGM interface is not shown explicitly in Figure 7, as this region is included in the CGM definition for this analysis. We find that the small variation of $f_{Z,CGM}$ with respect to stellar mass explained above persists regardless of whether this interface region is included or excluded from the CGM. However, for completeness, we report these values here. For log $(M_*/M_\odot) > 8.0$ galaxies, the disk–CGM interface typically retains $f_{Z,interface} = 0.069 \pm 0.035$; similarly, for log $(M_*/M_\odot) < 8.0$ galaxies, the interface typically retains $f_{Z,interface} = 0.081 \pm 0.043$. If we exclude this region from the CGM, this lowers the CGM retention to 0.19 ± 0.06 for log $(M_*/M_\odot) > 8.0$ galaxies and 0.15 ± 0.09 for log $(M_*/M_\odot) < 8.0$ galaxies.

4.3. Budgets By CGM Temperature Phases

The previous sections have quantified the mass and metal budget for the entire halo in the M+M sample. This section seeks to understand how the CGM mass and metal budgets are partitioned by temperature phases. For this section and the rest of this work, we define specific temperature regimes as follows:

1. Cold gas: $T < 10^{3.8}$ K.
2. Cool gas: $10^{3.8} < T < 10^{4.5}$ K.
3. Warm gas: $10^{4.5} < T < 10^{5.5}$ K.
4. Hot gas: $T > 10^{5.5}$ K.

We adopt these definitions based on the physical properties of the CGM in the M+M sample (see Section 5, Figure 10) and previous theoretical CGM work (e.g., S. Roca-Fàbrega et al. 2019) and reviews (e.g., J. Tumlinson et al. 2017).

Additionally, the previous section aimed to understand the contributions to the mass and metal budget from all regions within the halo (i.e., the disk, disk–CGM interface, and CGM). This section solely focuses on the CGM ($0.15R_{200c} > r > 1.0R_{200c}$).

CGM mass budget. We find that in the M+M sample the vast majority of CGM mass resides in either the cool or warm phases. Figure 8 shows how the CGM mass is divided between these two dominant phases. For each galaxy, the percentage of CGM mass that is in the cool phase (blue hexagon) or warm phase (orange triangle) is shown as a function of stellar mass. We also show the sum of these median percentages of the two phases, which indicates the typical fraction of CGM mass that does not reside in either of these phases.

For log $(M_*/M_\odot) > 8.0$ halos, ~95% of CGM mass exists in the cool or warm phases, while the remaining mass is at hotter temperatures ($T > 10^{5.5}$ K). At the low-mass end (log $(M_*/M_\odot) < 8.0$), less than 2% of CGM mass resides in this hotter, $T > 10^{5.5}$ K phase, and >98% of CGM mass resides in the cool or warm phases. The lack of hot gas in low-mass halos is likely due to their shallower gravitational potential wells, which prevent the halo from effectively retaining this hot gas.

In this mass range, 50/64 galaxies in the M+M sample have CGM dominated by the warm phase. For high and intermediate virial masses ($M_{vir} \sim 10^{10-11} M_\odot$), a relatively constant fraction of 75% of the CGM resides in this warm phase. However, at the highest masses, the two phases begin to approach an equal contribution. This is likely due to the disk extending closer to the $0.15R_{200c}$ boundary with increasing

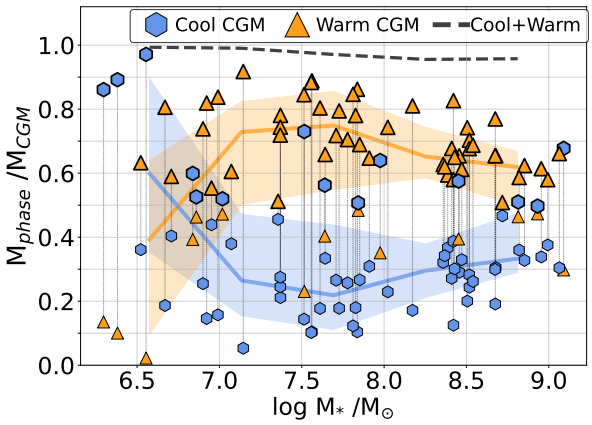

Figure 8. Fraction of CGM mass in the cool phase, $T = 10^{3.8}$–$10^{4.5}$ K (blue hexagons) and the warm phase, $T = 10^{4.5}$–$10^{5.5}$ K (orange triangles) as a function of stellar mass. For a given halo, the two phases are connected by a gray dashed line, and the dominant phase is bolded. The solid line and shaded region show the median CGM percent value and 16th–84th percentile range for the cool or warm phases in a bin size of 0.6 dex, plotted at the center of the bin. The dashed black line represents the sum of the median phase fractions, indicating the typical fraction of CGM mass not residing in the cool or warm gas phases (i.e., the cold or hot phases). The majority of CGM mass (>95%) resides in the cool and warm phases, and, for log$M_*/M_\odot > 7$ galaxies, the cool and warm CGM comprise a median value of 30% and 70% of CGM mass, respectively. Table 3 provides the mass in the cool and warm CGM phase for each galaxy in the M+M sample.

galaxy mass, which results in more cool, dense gas in the inner CGM (see Figure 10 and Appendix C). Additionally, at all masses there are halos with cool-dominated CGM. At lower masses, the fraction of warm CGM mass decreases considerably, and the cool phase approaches 100%. The sharp increase in cool phase percent is driven by the decrease in the virial temperature at this mass and the definitions of the CGM phases. Specifically, $M_* \leqslant 10^{6.5} M_\odot$ galaxies tend to reside in halos of virial masses below $M_{vir} \sim 10^{9.8} M_\odot$, which correspond to virial temperatures $T_{vir} \lessapprox 10^{4.5}$ K. With these virial temperatures, the CGM is generally unable to retain gas above this temperature (seen also in Figure 10) and the bulk of CGM mass resides in the cool phase. Ultimately, across virial masses the bulk of CGM mass resides near the virial temperature. Using particle tracking, we find the majority of this $T \sim T_{vir}$ phase was beyond R_{200c} at previous times, indicating this phase is primarily composed of IGM accretion.

CGM metal budget. The same method of determining metal retention introduced in Section 4.2 can also be done by further dividing the CGM into its two dominant temperature phases. Figure 9 shows the metal retention in the cool (blue squares) and warm (orange squares) CGM phases, and the total CGM retention (black lines) across stellar masses. The median values for galaxies binned by stellar mass are shown. For each median, the 16th–84th percentile range for the bin is shown as error bars (cold and warm phases) or shaded regions (total CGM). This figure selects all particles within $0.15R_{200c} < r < 1.0R_{200c}$, differing from Figure 7, which selected all particles $r_{\Sigma_{HI}} < r < 1.0R_{200c}$ (including the disk–CGM interface).

We find that, although there is variation in the median total CGM retention at different masses, there is no clear trend with stellar mass. Rather, the M+M sample shows a relatively flat CGM metal retention rate between 15% and 20%. Similarly, the cold and warm median metal retention rates also remain between 5% and 10% across stellar masses. Notably, for each bin the median rates for the two phases are comparable, despite

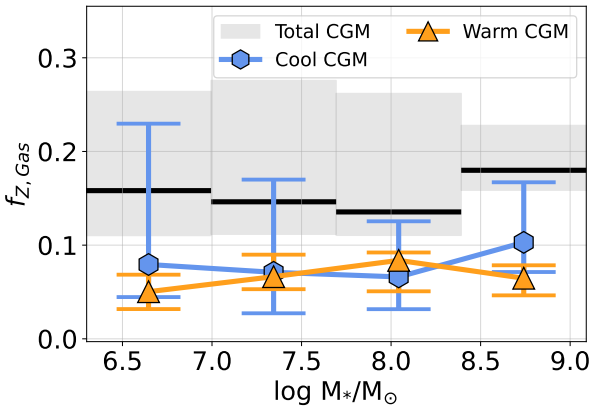

Figure 9. Metal retention in the cool (blue) and warm (orange) gas phases in the CGM ($r > 0.15R_{200c}$). The total CGM retention is shown as black bars and gray shaded regions. Shown are the median values for galaxies binned by stellar mass; the error bars/shaded regions denote the 16th–84th percentile range in that bin. We find similar fractions (5%–10%) are retained in the cool and warm phases, and across stellar masses a relatively consistent fraction is retained in the two phases and total CGM.

the two phases comprising different mass fractions of the CGM (Figure 8). The difference in mass fractions together with the similarity in metal retention indicates that the cool phase tends to consist of higher-metallicity material than the warm phase (also seen in Section 5, Figure 10), likely due to metals enhancing cooling rates into the cool phase and the warm phase being diluted by pristine IGM accretion.

5. Physical Properties of the CGM

The previous sections have demonstrated that dwarf galaxies in the M + M sample (1) contain a significant fraction of baryons in their CGM (∼50%) relative to their ISM and (2) retain 15%–20% of their metals in their CGM, and (3) that there is a prominent warm phase that constitutes the majority of the CGM mass budget. Having established that there is sufficient mass and metals for detection in the CGM, the physical conditions of this gas (temperature and density) will determine the ion fractions, therefore setting the abundance for a given species. Also, how the phase of the CGM depends on the distance from the galaxy will contextualize the column density profiles seen in Section 3.2. In this section, we show phase diagrams of the total CGM (gas density–temperature diagrams) and radial profiles for these properties, along with metallicity. Finally, in Section 5.2, we present the total mass accessible by UV spectroscopy as well as in individual ions.

The top row of Figure 10 shows the gas density–temperature phase diagrams. The three columns show particle data around galaxies in a given stellar mass bin according to the following ranges: $M_* = 10^{6.0-7.5}\,M_\odot$ (left column), $M_* = 10^{7.5-8.5}\,M_\odot$ (center column), and $M_* = 10^{8.5-9.5}\,M_\odot$ (right column); these are the same stellar mass bins as used in Figures 4 and 5.

The phase diagrams in the top row Figure 10 show the mass-weighted probability density for all gas particles around galaxies of the corresponding mass and within 0.15–$1.0R_{200c}$. The orange dashed line shows the median virial temperature for the galaxy mass bin, and black dashed curves show lines of constant pressure at 10^{-17}, 10^{-16}, and 10^{-15} Ba.

In the highest-mass galaxies, we find a substantial fraction of mass in a cool, dense phase ($n_{\rm gas} \sim 10^{-3}\,{\rm cm}^{-3}$, $T \sim 10^4$ K) and a warmer, more diffuse phase ($n_{\rm gas} < 10^{-4}\,{\rm cm}^{-3}$, $T > 10^{4.5}$ K). This bimodality is consistent with theoretical expectations for higher-mass galaxies (e.g., TNG50; see Figure 6 of D. Nelson et al. 2020) and existing work on lower-mass galaxies (e.g., FIRE; see Figure 11 of F. Li et al. 2021) in which the cooler gas is photoionized and the warmer component is a virialized component. Furthermore, the virialized component is largely composed of low-metallicity gas, likely due to dilution from pristine IGM accretion, as shown in the radial profiles described below.

Radial profiles with respect to normalized galactocentric radius (r/R_{200c}) of temperature, density, and metallicity are shown in the bottom three rows of Figure 10. The color bar shows the mass-weighted probability density (the same as the one used in the phase diagrams in the leftmost column). We highlight the CGM region ($0.15 < r/R_{200c} < 1.0$), which is demarcated by dashed lines, but also include the disk region ($r/R_{200c} < 0.15$) and the region immediately beyond the halo ($1.0 < r/R_{200c} < 1.6$).[15] For clarity, we also annotate each panel with the median properties of all particles within 0.15–$1.0R_{200c}$.

As shown in the temperature and density radial profiles (upper-middle and lower-middle rows of Figure 10), we find the cool component of the CGM is largely centralized to the inner regions of the halo, while the warmer phase exists in the outskirts. Similar to Auriga (A. W. S. Cook et al. 2025), FIRE-2 (J. Stern et al. 2021), and IllustrisTNG (R. Ramesh et al. 2025), we find a sharp transition from the cool to the warm phase at $r/R_{200c} \sim 0.4$. This transition in temperature roughly corresponds to the location where the cooling time becomes shorter than the free-fall time ($t_{\rm cool} < t_{\rm ff}$). This allows gas to cool to temperatures of $\sim 10^4$ K before falling into the galaxy on a free-fall time (e.g., J. Stern et al. 2021). The outer regions generally follow the virial temperature, which is in line with previous theoretical work predicting gas falling into a halo will be shock-heated to near the virial temperature (e.g., A. M. Brooks et al. 2009; F. van de Voort & J. Schaye 2012). Also, the cooling times in this outer region are longer than the free-fall times, which keeps the gas at near virial temperatures before falling into the galaxy. We find that the behavior of cooling and free-fall times in the M + M sample generally follows the behaviors seen in J. Stern et al. (2021); however, future work will investigate this more explicitly. Lastly, for all three galaxy mass bins, we find the hottest gas to have been recently heated by SNe feedback.

With decreasing mass, we find the inner CGM remains near $T \sim 10^4$ K, and the median gas density decreases. This occurs because with decreasing virial mass, the denser gas moves interior to our $0.15R_{200c}$ CGM definition (gray shaded region in Figure 10). We discuss the implications of our radial definitions in Appendix C. In the intermediate regions, decreasing halo mass leads to the transition between the cool and warm temperature phases moving inward toward the galaxy. In the outer regions, decreasing halo mass results in cooler temperatures in the outskirts owing to the lower virial temperatures. We also find that the gas density in the outskirts of the CGM remains near $n_{\rm gas} \sim 10^{-5}$–$10^{-5.5}\,{\rm cm}^{-3}$ for all halos.

Finally, the bottom row of Figure 10 shows metallicity profiles for the CGM in the M + M sample, relative to solar metallicity ($Z_\odot = 0.0134$; M. Asplund et al. 2009). We find the

[15] We choose to extend out to $1.6R_{200c}$, which is approximately R_{200m}, because some works choose to implement the R_{200m} virial definition as opposed to R_{200c}.

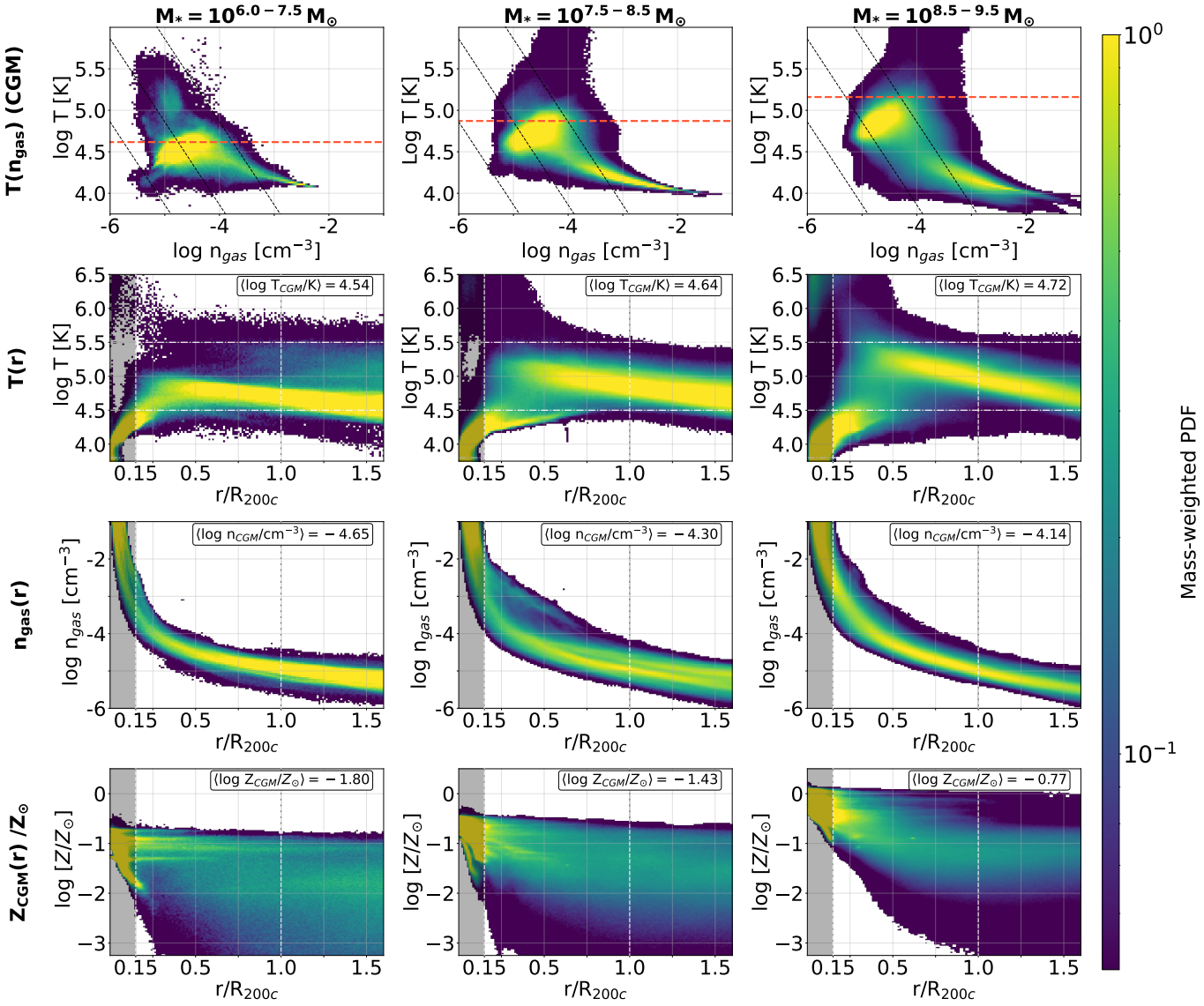

Figure 10. Physical properties of the gas within the halos of the M+M sample. Particle data are binned by stellar mass and plotted in the corresponding column (labeled on the top of each column) according to the following ranges: $M_* = 10^{6.0-7.5}\,M_\odot$ (left column), $M_* = 10^{7.5-8.5}\,M_\odot$ (center column), and $M_* = 10^{8.5-9.5}\,M_\odot$ (right column). Top row: gas density vs. temperature diagram ($T(n_{\rm gas})$) for only CGM particles (0.15–1.0R_{200c}). The orange dashed line represents the median virial temperature, while the black lines represent isobaric lines of 10^{-17}, 10^{-16}, and 10^{-15} Ba in thermal gas pressure. Also included are radial profiles as a function of normalized radial distance, r/R_{200c}, of gas temperature ($T(r)$, upper-middle row), gas density ($n_{\rm gas}(r)$, lower-middle row), and gas metallicity relative to solar ($Z(r)/Z_\odot$, bottom row). The gray shaded region denotes what is removed from the halo as the "disk," i.e., not included in the phase diagram. The color bar for all panels shows the mass-weighted probability density. The definitions for the various CGM temperature ranges are also shown in the $T(r)$ panels. Median conditions of the CGM ($r = 0.15$–$1.0R_{200c}$) are shown in each panel; we find that with decreasing mass, typical CGM conditions become more diffuse, cooler, and less metal-enriched. Median CGM density and temperatures for each galaxy in the M+M sample can be found in Table 3.

inner regions are the most metal-enriched for all galaxies, and the median CGM metallicity decreases with decreasing halo mass. Median gas metallicities relative to solar ($\log Z/Z_\odot$) at $r/R_{200c} = [0.25, 0.5, 1]$ are as follows:

1. $M_* = 10^{6.0-7.5}\,M_\odot$: $[-1.23, -1.65, -2.55]$.
2. $M_* = 10^{7.5-8.5}\,M_\odot$: $[-1.11, -1.44, -1.90]$.
3. $M_* = 10^{8.5-9.5}\,M_\odot$: $[-0.50, -0.88, -1.26]$.

We note that the metallicity of gas immediately inside and just beyond R_{200c} is similar and that there is no clear change in metallicity at either of these boundaries. The extent of metal-enriched gas implies that feedback is efficient at driving metals out of the disk, into the outer CGM and beyond the halo, likely beyond $1.6R_{200c}$ as well.

5.1. Ionization Fractions

The physical conditions of the CGM gas determine the ion fractions for each species. Figure 11 shows the median ion fractions ($f_{\rm ion}$) calculated using CLOUDY (assuming the F. Haardt & P. Madau 2012 UV photoionizing background) for H I as well as a low metal ion, C II, intermediate metal ion, C IV, and high metal ion, O VI. Each ion shows three curves corresponding to the same three mass bins used in Figure 10. We find that the most suitable conditions (cool, $T < 10^{4.5}$ K, and dense, $n_{\rm gas} > 10^{-3}\,{\rm cm}^{-3}$) for species with lower ionization potentials (e.g., H I and C II) are in the inner CGM. Both $f_{\rm HI}$ and $f_{\rm CII}$ fall off steeply with increasing values of r/R_{200c}; however, for $r/R_{200c} > 0.5$, $f_{\rm HI}$ remains near a consistent value.

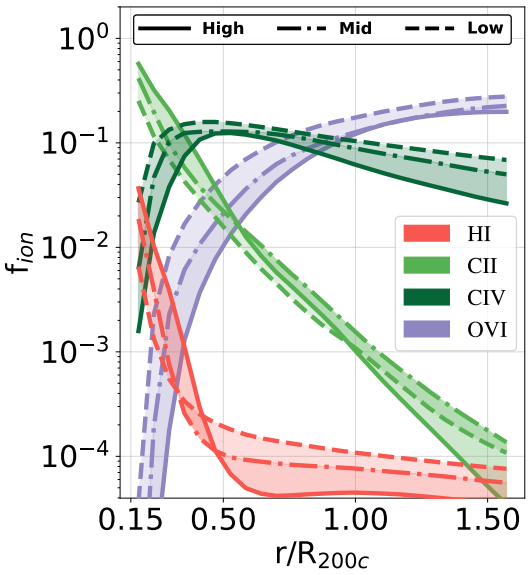

Figure 11. Ion fractions ($f_{\rm ion}$) for H I (salmon) and a representative low ion (C II, light green), intermediate ion (C IV, dark green), and high ion (O VI, purple) as a function of radial separation from the galaxy. For each ion, we show the median values for the same three virial mass bins as Figure 10, with solid, dashed–dotted, and dashed lines representing high-, intermediate-, and low-mass galaxies. We see little variation in the shape of $f_{\rm ion}$ radial profiles with halo mass. However, with increasing distance from a galaxy, low ions (H I and C II) become increasingly less abundant and intermediate/high ions (C IV and O VI) become the dominant ionization stages; this is due to the radial dependence of the CGM's physical properties (Figure 10).

We find the intermediate ions (C IV) are most prominent in the intermediate regions ($r/R_{200c} \sim 0.5$) and show a flatter ion fraction profile. $f_{\rm CIV}$ is greatest in regions of intermediate densities ($10^{-3} < n_{\rm gas} < 10^{-5}\,{\rm cm}^{-3}$) and warmer temperatures ($10^{4.5} < T < 10^{5.0}$ K). For the higher ion, $f_{\rm OVI}$ is greatest in regions of similar temperature to $f_{\rm CIV}$ ($10^{4.5} < T < 10^{5.0}$ K) but more diffuse ($n_{\rm gas} < 10^{-5}\,{\rm cm}^{-3}$). Additionally, $f_{\rm OVI}$ peaks beyond R_{200c}, which indicates there is likely a significant portion of O VI mass just outside the halo. Observations of O VI column densities are thus likely to detect a significant portion of O VI that exists beyond R_{200c}. These results are consistent with observed radial trends (e.g., S. D. Johnson et al. 2015; N. Mishra et al. 2024), and comparable to trends found in FIRE simulations (F. Li et al. 2021).

When comparing galaxies of different virial masses, we find little variation in the qualitative behavior of $f_{\rm ion}$ (i.e., $f_{\rm CII}$ always peaks in the innermost regions while $f_{\rm OVI}$ has a maximum beyond R_{200c}). However, the conditions in which the various ions are most prominent by mass do vary slightly with virial mass based on the availability of material at certain densities and temperatures. For instance, high-mass galaxies have more mass in C IV at $T > 10^{5.0}$ K than low-mass galaxies, given that low-mass galaxies have very little CGM mass at $T > 10^{5.0}$ K. Nonetheless, the similarity of $f_{\rm ion}$ across virial masses indicates that the change in column densities with respect to galaxy mass (comparing panels within a given row) seen in Figures 4 and 5 is more strongly driven by the change in CGM gas and metal mass than the change in the phase of the CGM phase seen in Figure 10. However, the change in column densities from ion to ion within a given mass bin (comparing panels within a given column) is driven by the multiphase structure of the CGM seen in Figure 10.

5.2. UV-observable Budget

Ultimately, the total gas mass and ion fractions of the CGM will determine the total mass of a given ion. In this section, we characterize the total mass of individual ions in the CGM and the total mass that is accessible in the UV. This analysis provides benchmarks for estimating how much of the CGM mass is probed by UV absorption spectroscopy, and allows for better comparisons to other simulations.

The left panel of Figure 12 shows the masses of individual ions (H I, C II, C IV, Si II, Si III, Si IV, and O VI) in the CGM in the M + M sample. Each point represents the median ion mass in the CGM around a galaxy within a given stellar mass bin, and the error bars represent the 16th–84th percentile range. The three mass bins are log $M_*/M_\odot$ = 8.5–9.5, log $M_*/M_\odot$ = 7.5–8.5, and log $M_*/M_\odot$ = 6.0–7.5, and are denoted on the horizontal axis. The mass in each ion trends with the stellar mass of the galaxy, in that the highest-mass galaxies tend to also have the most mass in each ion studied. We note, however, that, especially for the intermediate- and low-mass bins, there is substantial scatter in the total mass of ions, some as great as 1–2 dex.

The center panel of Figure 12 shows the median total mass in UV-observable hydrogen, silicon, carbon, and oxygen in the CGM for the same three stellar mass bins denoted on the horizontal axis. We define the UV-observable mass as the sum of ion masses that have transitions accessible by UV absorption spectroscopy at z = 0–0.3. More specifically, that is the total mass of H I for hydrogen; Si II, Si III, and Si IV for silicon; C II and C IV for carbon; and O VI for oxygen. The right panel of Figure 12 shows the fraction of the total element mass that is in UV-observable ions (i.e., $f_{\rm C} = (M_{\rm CII} + M_{\rm CIV})/M_{\rm C}$) for the same elements and stellar mass bins. The fraction of UV-observable mass can also act as an ionization correction for observational studies that estimate the total element mass using a set of UV-observable ions (e.g., Y. Zheng et al. 2024). For convenience, we list for each element the median values and associated 16th–84th percentile ranges for the fraction of UV-observable mass in Table 2.

We find that higher-mass galaxies tend to contain the largest amount of mass that is accessible in the UV. With decreasing stellar mass, the total element mass and total UV-observable mass in each element decrease. Similarly, the percentages generally tend to also decline. The fraction of oxygen that is accessible in the UV does increase toward the low-mass end, however the change is on the 1% level. The oxygen UV-observable budget is small (<10%) for galaxies across stellar masses due to a large fraction of O VI mass residing at or beyond the R_{200c} boundary and the majority of the oxygen mass existing in other ionization stages (see Section 6.1 for more details).

6. Discussion

6.1. Underpredicted Column Densities

In this subsection, we present a brief investigation into the ions that are in the weakest agreement with observations (O VI and C IV), and assess what may be driving the underprediction of these ions seen in Figure 5.

O VI column densities. $N_{\rm OVI}$ shows the weakest agreement with observations across all ions covered in this work, with 0/6 detections lying within 2σ of the M + M sample medians. As noted in Section 3, the O VI observations included in this work are at systematically higher redshifts. A brief investigation into

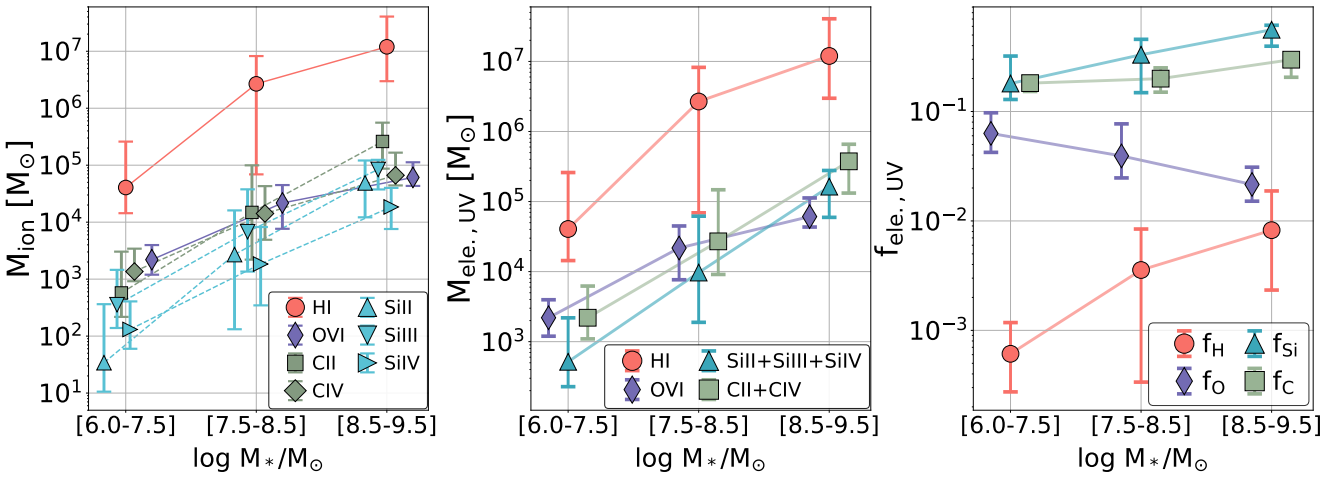

Figure 12. CGM UV-observable (at $z = 0$–0.3) budgets for the M+M sample. Left panel: median masses of individual ions with UV-detectable transitions in the CGM. Center panel: median total UV-observable mass in the CGM ($M_{ele.,UV}$), defined as the summed mass of ions with UV-detectable transitions (explicitly written in the legend and plotted in the left panel). Right panel: corresponding UV-observable fraction/ionization correction ($f_{ele.,UV}$), defined as the UV-observable mass divided by total element mass ($f_{ele.,UV} = M_{ele.,UV}/M_{ele.}$). Each panel shows results for three stellar mass bins (log $M_*/M_\odot$ = 6.0–7.5, 7.5–8.5, and 8.5–9.5), and the error bars show the 16th–84th percentile range; markers are horizontally offset for clarity. Elements are represented as follows: hydrogen (salmon circles), silicon (blue squares), carbon (green triangles), and oxygen (purple diamonds). In the left panel, markers are rotated to distinguish between ions.

the simulated N_{OVI} across redshifts ranging from $z = 0$ to 1 revealed that these column densities can indeed change with redshift; however, for a given galaxy, the columns may increase or decrease within 0.5 dex with decreasing redshift. Notably, an increase of 0.5 dex is too small a change to match the observations shown in Figure 5, and thus the M+M sample likely underestimates O VI even at redshifts consistent with current observations.

Since the change in N_{OVI} with redshift cannot produce columns in agreement with observations, the underprediction of N_{OVI} is likely due to one or both of (a) a lack of metals in the outer CGM, and (b) a lack of material in the correct phase. Previous work for high-mass galaxies has shown that BH feedback can strongly shape the O VI content in the CGM and enhance column densities in O VI by pushing more metal-enriched material out to the CGM outskirts (e.g., D. Nelson et al. 2018; N. N. Sanchez et al. 2019, 2021). The change in simulated N_{OVI} values revealed by this brief investigation implies a dependence on both redshift and galaxy activity. Thus, a similar explanation may apply to our simulations, such that increased SNe feedback in our dwarf galaxies could lead to O VI column densities in better agreement with observations.

The underprediction of O VI and agreement of low ions and Si IV may also point to our simulations underproducing a certain gas phase. We investigate this by finding the mass in individual ionization states within 140 kpc of each galaxy (approximately the observed region probed by the synthetic sightlines). Relative to O VI mass, we find that there is significant mass in all ionization states O II through O VII. For log $(M_*/M_\odot) > 8.0$ galaxies, there is 1–3× as much mass in O V and O VII as there is in O VI (e.g., M_{OV}/M_{OVI} = 1–3) and 1–7× as much mass in O II, O III, and O IV. For log $(M_*/M_\odot) < 8.0$ galaxies, this ratio declines, but there is still 1–2× as much mass in O V, O IV, and O VII. These results suggest that the underprediction of N_{OVI} is likely strongly driven by a bulk of CGM mass residing in different ionization states than O VI.

C IV column densities. Similarly, our N_{CIV} results tend to be below current observations (0/8 and 5/8 detections within 1σ and 2σ, respectively). We perform a similar calculation as oxygen for carbon, and determine which ionization states hold the most mass within 140 kpc of each galaxy. For carbon, we also find significant mass in ionization states other than C IV. Specifically, across galaxy masses, we find there is 4–6× as much mass in C V and 1–3× as much mass in C VI relative to C IV (e.g., M_{CV}/M_{CIV} = 4–6). Also, there is significant mass in C III, with 3–6× and 1–2× more mass than C IV for high-mass and low-mass galaxies, respectively.

Relative to lower ions, O VI and C IV are typically expected to be prominent in warmer and more diffuse material (see Figure 3). Thus, the M+M sample likely underpredicts warm and diffuse material (where ionization fractions peak in O VI and C IV) in the outer regions of the halo while still producing enough cooler material in the central regions of the halo to match the observations of H I, low ions, and Si IV. However, previous work (see above) has also pointed to a correlation between N_{OVI} and feedback processes, suggesting that stronger feedback may also increase N_{OVI} values in the M+M sample.

Future works will investigate the properties of O VI in the M+M sample at higher redshifts and the effects on the CGM-DG from including additional physics, aiming to further disentangle which of the above scenarios is producing the low O VI column densities seen in this work.

Table 2
Summary of f_{UV} for Hydrogen, Carbon, Oxygen, and Silicon

	Low M_* $10^{6.0-7.5}$ $M_\odot$	Mid M_* $10^{7.5-8.5}$ $M_\odot$	High M_* $10^{8.5-9.5}$ $M_\odot$
Hydrogen	$0.06^{+0.06}_{-0.03}$%	$0.36^{+0.49}_{-0.32}$%	$0.82^{+1.06}_{-0.59}$%
Carbon	$18.2^{+1.4}_{-2.9}$%	$20.0^{+5.1}_{-4.9}$%	$29.8^{+3.9}_{-9.2}$%
Oxygen	$6.3^{+3.4}_{-2.1}$%	$3.9^{+3.8}_{-1.5}$%	$2.2^{+0.9}_{-0.6}$%
Silicon	$18.0^{+14.1}_{-5.1}$%	$33.0^{+12.7}_{-18.1}$%	$55.9^{+5.5}_{-16.4}$%

Note. Each value presented is the median and 16th–84th percentile ranges. The values provided here are the same as those plotted in the left panel of Figure 12 and duplicated for convenience.

6.2. Tying CGM Column Densities to CGM Structure

In addition to comparing our mock column densities to observed values, we interpret them in the context of the CGM structure. In Section 3, Figures 3, 4, and 5, we observe a steep inner $N_{\rm HI}$ profile followed by a plateau in the outer CGM—most pronounced for galaxies with $\log(M_*/M_\odot) > 7.5$. We argue that this behavior results from the radial temperature and density profile of the CGM, which is evident when determining the individual contributions from the cool and warm phases to each $N_{\rm HI}$ value. By selecting all particles along a single line of sight within a given temperature range, we calculate the $N_{\rm HI}$ from that single phase. We find the cool CGM contribution dominates over the warm phase within $b/R_{200c} < 0.5$, reaching $N_{\rm HI} = 10^{18}\,{\rm cm}^{-2}$. However, with increasing b/R_{200c}, the cool phase column density falls off steeply. This decline mirrors the behavior of $f_{\rm HI}$ in Figure 11, which is driven by the declining cool gas mass with increasing r/R_{200c} (Figure 10). Beyond $\sim 0.5R_{200c}$, the absence of dense, $T \sim 10^4$ K gas causes the contribution from the cold phase to fall off, while that from the warm phase becomes dominant.

Across all b/R_{200c}, the warm phase contributes $\sim 10^{14}\,{\rm cm}^{-2}$ to each $N_{\rm HI}$. We can interpret the relatively constant warm phase contribution to $N_{\rm HI}$ using Figure 11, where $f_{\rm HI}$ plateaus for $r/R_{200c} > 0.5$ and the warm phase dominates. The combination of this flat $f_{\rm HI}$ and the substantial mass in the warm phase (Figure 8) leads to the warm phase contributing $\sim 10^{14}\,{\rm cm}^{-2}$ to the total $N_{\rm HI}$ across all impact parameters. Once the cool phase contribution falls off at greater b/R_{200c}, the warm phase's consistent $N_{\rm HI} \sim 10^{14}\,{\rm cm}^{-2}$ dominates and produces the $N_{\rm HI}$ plateau.

Similarly, low ions like C II, Si II, and Si III also peak in cool, dense gas, and thus the same physical reason for the steep inner profile of $N_{\rm HI}$ also gives rise to the steep low ion profiles. These ions have ion fractions that fall off rapidly with r/R_{200c} (Figure 11); however, due to these ions having significantly less mass than H I, the column density does not plateau above detectable limits.

By mass, the intermediate ion C IV is most abundant in the intermediate regions of the CGM ($b/R_{200c} \sim 0.5$), with the majority of C IV mass residing between 0.25 and $0.5R_{200c}$. Given that C IV is most abundant in the intermediate regions, the $N_{\rm CIV}$ profile is less steep than lower ions and shows a flatter decline with b/R_{200c}, seen in Figures 3 and 5. Finally, a similar explanation can also be used to explain the flat $N_{\rm OVI}$ profile, since the O VI ion fractions peak beyond the halo.

6.3. Comparison to Previous Work

Previous work studying the simulated CGM-DG has found qualitatively similar column density profiles as we find here. Specifically, $N_{\rm HI}$ profiles with a clear plateau beyond $b \sim 0.5R_{200c}$ have been found in previous work (e.g., T. A. Gutcke et al. 2017; M. Mina et al. 2021; A. W. S. Cook et al. 2025), as well as steep $N_{\rm SiII}$ profiles dropping below detectable limits before $b \sim 0.5R_{200c}$ (e.g., M. Mina et al. 2021; A. W. S. Cook et al. 2025). We find similar O VI column densities below current observations as NIHAO (T. A. Gutcke et al. 2017), which investigated the H I and O VI CGM content in a wide range of galaxies. However, at $b \sim 0.5R_{200c}$, we find lower O VI column densities by $\sim$0.5 dex compared to M. Mina et al. (2021; which studied the "Seven Dwarfs" simulations ran with GASOLINE2; see J. W. Wadsley et al. 2017), despite our works showing similar numerical results when comparing H I and C IV column densities. M. Mina et al. (2021) examined differences in the CGM for a set of simulated galaxies[16] run with both BW and SB feedback models. They found that the BW O VI column densities are $\sim$1 dex lower than the SB O VI column densities. Although we do not see a clear trend in O VI between suites in the M+M sample (see Appendix B), future work will investigate further how the CGM changes when altering SNe feedback.

Similarly, at $b \sim 0.5R_{200c}$, around $\log(M_*/M_\odot) > 8.5$ dwarf galaxies the M+M sample produces higher column densities than Auriga (A. W. S. Cook et al. 2025) in both C IV (M+M, $N_{\rm CIV} \sim 10^{13}\,{\rm cm}^{-2}$; Auriga, $N_{\rm CIV} < 10^{11}\,{\rm cm}^{-2}$) and O VI (M+M, $N_{\rm OVI} \sim 10^{13}\,{\rm cm}^{-2}$; Auriga, $N_{\rm OVI} < 10^{11}\,{\rm cm}^{-2}$). These lower values of $N_{\rm CIV}$ and $N_{\rm OVI}$ are likely due to the Auriga galaxies having much lower metallicities in the outer CGM, where these ions would preferentially exist, than the M+M sample. Specifically, A. W. S. Cook et al. (2025) show that beyond $r/R_{200c} \sim 0.25$ the CGM of $M_{200c} = 10^{10.0} M_\odot$ and $10^{10.5} M_\odot$ galaxies in Auriga has metallicities $\log Z/Z_\odot < -3$. The authors note that the low metallicity in the outer regions of the halo is caused by the outflows from the dwarf galaxies not reaching larger distances, as evidenced by an average outflow radial velocity of $\sim$0 km s^{-1} at $r/R_{200c} \sim 0.25$. This implies that the M+M sample dwarf galaxies are more efficient at dispersing metals into the full extent of the CGM and beyond the halo, and this fact is critical in producing greater $N_{\rm CIV}$ and $N_{\rm OVI}$.

We also compare our mass and metal retentions to previous works. The total halo mass retention rates for the M+M sample are roughly in agreement with those presented in Z. Hafen et al. (2019; FIRE-2) and C. R. Christensen et al. (2016), peaking at around $\sim$60% for the highest-mass dwarf galaxies and dropping to $\sim$10% at the lowest masses. However, the metal retention rates do differ between these works. Z. Hafen et al. (2019) find in FIRE-2 that at all halo masses, $z = 0.25$ dwarf galaxies have lost $\sim$40% of their metals from the halo. Notably, this work claims a relatively flat fraction of metals lost from the halo, $f_{\rm Z,lost}$. However, the M+M sample and C. R. Christensen et al. (2018) show an *increasing* $f_{\rm Z,lost}$ with decreasing mass (as indicated by the "Z Lost" diagonal lines in Figure 7).[17] For the same range of halo masses as Z. Hafen et al. (2019), C. R. Christensen et al. (2018) find $f_{\rm Z,lost} = 30\%$–70%, while in the M+M sample $f_{\rm Z,lost} = 0\%$–70%. Although the M+M sample loss rates differ at the high-mass end compared to C. R. Christensen et al. (2018), we note that we utilize a larger number of galaxies and observe a fair degree of scatter in metal-loss rates. When instead considering the median loss rates for the M+M sample, we find $f_{\rm Z,lost} = 19 \pm 10\%$ for $M_{200c} \sim 10^{10.5-11.0} M_\odot$ galaxies and $f_{\rm Z,lost} = 51 \pm 15\%$ for $M_{200c} \sim 10^{10.0-10.5} M_\odot$ galaxies, more in agreement with C. R. Christensen et al. (2018). As noted in C. R. Christensen et al. (2018) and Z. Hafen et al. (2019), the differences in $f_{\rm Z,lost}$ across

[16] In fact, the "Seven Dwarf" simulations presented in M. Mina et al. (2021) use the same initial conditions as our "cptmarvel," part of the Marvel-ous Dwarfs suite, but ran with GASOLINE2 instead of CHANGA.

[17] We note that C. R. Christensen et al. (2018) used GASOLINE (J. W. Wadsley et al. 2004), which is a predecessor to CHANGA. GASOLINE and CHANGA implement similar star formation parameters and a BW feedback model. However, CHANGA is designed to scale more efficiently and uses the hydrodynamics methods from GASOLINE2 (J. W. Wadsley et al. 2017).

simulations are likely due to differences in feedback prescriptions, as the feedback mechanisms will have a dominant role in dispersing metals into the CGM and IGM. However, further work is needed to understand the origin of the differences in detail.

Similar to the M+M sample, the CGM-DG in EAGLE (Y. Zheng et al. 2024) finds the metal mass in the cool and warm phase are roughly equal. Although both suites find this equipartition in metals between phases, in terms of total gas mass, the CGM-DG in EAGLE is more strongly dominated by the warm phase than the M+M sample (EAGLE contains >7 times as much mass in the warm phase as cool, compared to the M+M sample containing ∼3 times in the warm phase). In both the M + M sample and EAGLE, the cold phase retains ∼10% of the metals produced by the galaxy. This roughly equal distribution in metals between gas phases is not found in FIRE (A. L. Muratov et al. 2017), which finds that most metals reside in the cooler temperature range, $10^4 < T < 10^{4.7}$ K. This may suggest that more cool gas is ejected in the FIRE runs than in the M + M sample or EAGLE. Note that A. L. Muratov et al. (2017) studied FIRE-1 galaxies, which did not include metal mixing, and might lead to higher metallicity in ejected cool gas and enhanced cooling in the CGM. Z. Hafen et al. (2019) note that the overall metal content of the CGM is consistent between FIRE-1 and FIRE-2, however.

In terms of the physical properties of the CGM, the M + M sample, FIRE-2 (F. Li et al. 2021), and EAGLE (Y. Zheng et al. 2024) find a prominent warm ($T > 10^{4.5}$ K) and diffuse ($n < 10^{-3}$ cm^{-3}) component for $r > 0.5R_{200c}$ CGM gas around $7.5 \leqslant \log(M_*/M_\odot) \leqslant 9.5$ galaxies. However, in the same regions, FIRE also produces a cool ($T \leqslant 10^{4.0}$ K) and dense ($n > 10^{-1}$ cm^{-3}) component which is not present in the M + M sample. Again, this effect may indicate that feedback in FIRE-2 galaxies couples stronger with the ISM gas and is more effective at pushing cool, dense gas into the outer regions of the CGM. Across galaxy masses, the majority of CGM mass in the M + M sample exists at temperatures within $T \sim 10^{4.5}$–$10^{5.5}$ K. In contrast to these other studies, P.-C. Tung & K.-J. Chen (2025), which studied dwarf galaxies in an increased resolution run of IllustrisTNG (∼100× higher resolution than the fiducial suite), finds the majority of CGM gas exists within $T \sim 10^3$–10^4 K. The authors suggest this preferentially colder CGM is due to the higher resolution of their simulations, increasingly resolving cold gas structures, though it is surprising that a substantial amount of gas is below the virial temperature of the halos.

6.4. Limitations

In this section, we discuss the potential limitations of our results based on the effects of the force and mass resolution limits and feedback physics not included in our simulations.

Both the Marvelous Dwarfs and Marvelous Massive Dwarfs suites have comparable force resolutions, both <100 pc. As our analysis of the CGM-DG tends to focus on global properties integrated over halo scales (∼100 kpc), the results presented in this work are operating well above the physical length scale resolution limits.

In regards to the mass resolution, previous observational works have posited that the CGM may comprise low ions existing in subkiloparsec clumps of cool/cold gas embedded in a warmer medium (e.g., W. H. Hsu et al. 2011; M. McCourt et al. 2018; F. S. Zahedy et al. 2019; R. Augustin et al. 2021; Y. Zheng et al. 2024). Previous theoretical works from other simulations found that increased mass resolution increases the number of these cool clouds and affects their geometry (e.g., M. S. Peeples et al. 2019; R. Ramesh & D. Nelson 2024) and increases the overall cool gas content of the CGM (e.g., C. B. Hummels et al. 2019; M. S. Peeples et al. 2019; F. van de Voort et al. 2019; M. P. Rey et al. 2024). Among the effects of increased mass resolution on the cold CGM, the GIBLE project (IllustrisTNG; R. Ramesh & D. Nelson 2024) finds the cold gas fraction and mass in the CGM are converged properties when improving the cell mass resolution in the CGM from $m_{\rm gas,CGM} \sim 8.5 \times 10^5\,M_\odot$ to $m_{\rm gas,CGM} \sim 1.8 \times 10^3\,M_\odot$—comparable gas mass resolutions to the Marvelous Dwarfs and Marvelous Massive Dwarfs suites, and comparable to C. B. Hummels et al. (2019).

With increasing mass resolution, the column densities in low ions may increase by as much as a factor of 2 (e.g., H I in C. B. Hummels et al. 2019; F. van de Voort et al. 2019). However, work using FOGGIE suggests these column densities only marginally change (within 10%–20%) when increasing CGM resolution (e.g., M. S. Peeples et al. 2019). For this work, the little variation in column densities and cool/warm gas fractions between suites in the M + M sample, despite differences in gas mass resolution, suggests that increased mass resolution could marginally increase our column densities but will have a greater effect on the substructure of the CGM, similar to results in M. S. Peeples et al. (2019) and R. Ramesh & D. Nelson (2024).

Additionally, theoretical work focusing on Milky Way–mass galaxies has demonstrated that the inclusion of cosmic-ray (CR) feedback can alter the CGM (e.g., I. S. Butsky et al. 2022). Although our simulations do not include CR physics, work done in the FIRE group predicts that the pressure support from CRs likely only becomes important for $M_{\rm vir} \geqslant 10^{12}\,M_\odot$ galaxies (S. Ji et al. 2020). Furthermore, F. Li et al. (2021) found the inclusion of CRs in FIRE dwarfs only slightly enhanced the equivalent width in O VI. In IllustrisTNG, it has been shown that CRs largely do not alter the density, temperature, and total pressure in the CGM-DG. However, varying strengths of CR feedback can alter star formation (R. Ramesh et al. 2025). In both IllustrisTNG and in FIRE, the effect is strongest for Milky Way–mass galaxies (suppressing star formation by a factor of ∼10), but for $M_* \sim 10^9\,M_\odot$ dwarf galaxies star formation can be suppressed by a factor of ∼2, and approaches unity with decreasing mass (R. Ramesh et al. 2025). Although the M + M sample lacks CR feedback, the aforementioned studies suggest that this feedback mechanism plays a less significant role in the low-mass CGM/galaxy evolution compared to its impact on higher-mass systems.

Lastly, in generating ionization fractions, we model the UV photoionizing background (UVB) using the F. Haardt & P. Madau (2012) metagalactic radiation field. Previous work has demonstrated that the F. Haardt & P. Madau (2012) field underpredicts H I photoionization (e.g., C.-A. Faucher-Giguère 2020). As such, adopting a different photoionizing background would likely increase the low ion content in our simulations. Further, we assume that the radiation from the central galaxy is negligible. Although this assumption is motivated by the low star formation rates seen in Figure 2, the existing literature has begun to indicate that explicitly modeling ionizing radiation from stars can affect CGM properties around Milky Way–mass galaxies. For instance,

B. Baumschlager et al. (2024) implemented an "on-the-fly" radiative transfer (RT) model in GASOLINE2 which discretizes the radiation field at discrete photon energies. The authors found the inclusion of RT in modeling the radiation from the UVB and local stars results in a significant increase in H I mass in the ISM and CGM (see Figure 1 in B. Baumschlager et al. 2024). Furthermore, B. Baumschlager et al. (2025) find that for the same dwarf galaxies as used in M. Mina et al. (2021), RT resulted in a nonnegligible impact on ions like CIV. Ultimately, the inclusion of RT in the M+M sample could alter the abundance of species like H I, C IV, and O VI.

6.5. Observability of the CGM of Dwarf Galaxies

The M+M sample can be leveraged to provide theoretical expectations for future CGM-DG observations. In this section, we cover the halo and stellar mass dependence of the CGM and its implications for observations. We organize the following section by galaxy mass, beginning with our interpretations for low-mass dwarf galaxies and moving up the mass scale.

Low-mass dwarf galaxies. We find the CGM of $M_* = 10^{6.0-7.5}\,M_\odot$ galaxies exhibits a less multiphase structure compared to its higher-mass counterparts (Figure 10). The majority of mass beyond $0.15R_{200c}$ resides in cool ($10^4 < T/\mathrm{K} < 10^{4.6}$), diffuse ($n_{\rm gas} < 10^{-4}\,\mathrm{cm}^{-3}$), and low-metallicity material in the outskirts of the CGM ($r > 0.5R_{200c}$). Since this material in the outer CGM is very diffuse, the ion fractions for low ions are small (Figure 11) despite being at cooler temperatures. For higher ions like C IV and O VI, the gas conditions are suitable for high ion fractions, but the lack of mass and metals (Figures 6 and 7) in these systems limits the amount of UV-observable mass. Specifically, the CGM in this mass regime only has $\sim 10^3 M_\odot$ of silicon, carbon, or oxygen mass that is accessible with UV spectroscopy (Figure 12). Ultimately, the small amount of mass in UV-accessible ions leads to columns below the detection threshold in the vast majority of ions (Figures 4 and 5). Thus, metals in the CGM of $M_* = 10^{6.0-7.5}\,M_\odot$ galaxies are largely below current detection limits. However, within $b/R_{200c} < 0.2$, metal column densities may be detectable. Assuming the M+M sample does produce realistic CGM, future observations targeting $M_* = 10^{6.0-7.5}\,M_\odot$ galaxies will likely need to observe the CGM within ∼4–5 kpc of the disk to detect metal ions such as C II, C IV, Si II, and Si III.

High-mass dwarf galaxies. The CGM of $M_* = 10^{8.5-9.5}\,M_\odot$ dwarf galaxies shows a highly multiphase structure with 60%–75% of its mass in the warm/virialized phase, 30%–40% in the cool/photoionized phase, and <5% in a hot phase comprising recently SNe-heated and ejected gas (Figures 8 and 10). These galaxies have typically retained a larger fraction of the metals produced (80%–100%) within their halo as compared to lower-mass galaxies (Figure 7). Although the majority of the metals produced are within the disk region (40%–80%), and primarily in the gas phase, the CGM of these galaxies retains a nonnegligible fraction of metals (20%–40%). We find the budget of UV-observable CGM mass is greatest for these galaxies, with ∼32% of carbon mass and ∼60% of silicon mass existing in UV-accessible ions (Figure 12 and Table 2). However, only ∼2% of oxygen mass is in O VI, while there is >2× as much mass in other ionization stages like O II through O V and O VII (see Section 6.1). Given the masses of UV-observable ions, most ions studied are above detectable limits within $0.5R_{200c}$, but at greater distances, column densities (especially in low ions) are below detectable limits, in agreement with observations. For low ions, the decrease in column densities is due to declining ion fractions because of warmer and more diffuse conditions in the outer CGM regions. For this mass range, the M+M sample produces CGM column densities in broad agreement with observations (⩾90% of detections are within 2σ). Assuming the M+M sample does produce realistic CGM, we predict future observations will continue to find detections of low ions and C IV within 40–50 kpc of the galaxy. However, these lower ions do not probe the majority of the CGM mass residing in the virialized phase, which retains a comparable fraction of metals to the cool phase (∼10%; Figure 9).

7. Summary

In this work, we use two suites of cosmological zoom-in simulations to study the CGM of dwarf galaxies. We select a sample of 64 isolated, $z = 0$ dwarf galaxies within the stellar mass range $6.0 \leqslant \log(M_*/M_\odot) \leqslant 9.5$, referred to as the M+M sample. We compare to current observations by deriving synthetic column densities in various ions, and characterize the CGM by investigating its mass and metal retention, as well as various physical properties. Ultimately, we find as follows:

1. The M+M sample produces synthetic column densities in broad agreement with current observations included in Y. Zheng et al. (2024) and a subsample of those presented in N. Mishra et al. (2024). Generally, $M_* > 10^8\,M_\odot$ dwarf galaxies have CGM that can be observed in both H I and metal ions. While the CGM of lower-mass dwarf galaxies can be observed in H I, the metal ions studied show column densities below detectable limits, likely due to large rates of metal loss from the CGM (Figure 7).
   (a) In the most massive dwarf galaxies, $N_{\rm HI}$ shows a steeply declining inner CGM profile and a flat outer CGM profile that plateaus at $\sim 10^{14}\,\mathrm{cm}^{-2}$. With decreasing mass, the inner profile becomes less steep while the outer plateau value remains around $\sim 10^{14}\,\mathrm{cm}^{-2}$. We argue this profile is due to the density and temperature profile of the CGM setting the ionization fractions of H I (see Section 6.2 and Figures 10 and 11).
   (b) Low ions (Si II, Si III, C II) have a steeply declining profile that falls well below detectable limits by $0.5\,R_{200\,c}$. This trend is in agreement with published observations, where these ions are only observable at low impact parameters ($b/R_{200\,c} < 0.5$). We argue this steep decline in column density is due to the CGM becoming warmer at greater values of $r/R_{200\,c}$, leading to the decline in ionization fractions of these low ions (Figures 10 and 11).
   (c) The intermediate ion C IV does not have a column density profile that falls off as rapidly as lower ions. The shallower $N_{\rm CIV}$ profile is due to C IV preferentially existing in the warmer, intermediate regions of the halo ($r/R_{200\,c} \sim 0.5$) where its ionization fractions peak (Figure 11). The M+M sample reproduces 0/8 and 5/8published detections within $1\,\sigma$ and $2\,\sigma$, respectively. The lack of detections lying within $1\,\sigma$ of the simulated median

indicates the M+M sample likely underproduces C IV and overproduces higher ionization states of carbon (Section 6.1).

(d) The highest ion we include, O VI, has a flat column density profile because it exists predominantly beyond $R_{200\,c}$ where ionization conditions are most suitable (Figure 11). We find $N_{\rm OVI}$ values are less than all published detections at higher redshifts by $\sim$1 dex, indicating the M+M sample underpredicts the O VI-bearing phase. Similar to carbon, we find substantial mass in other ionization states of oxygen.

2. The CGM ($r/R_{200c} = 0.15$–1.0) in the M+M sample dominates the total baryonic budget for 58/64 galaxies (Figure 6). Across halo masses, the CGM tends to retain a consistent 15%–20% of metals produced (Figure 9). Although the CGM metal retention shows little variation with respect to the galaxy mass, the disk retention decreases with mass, and correspondingly the fraction of metals lost increases (Figure 7). With decreasing halo mass, the median CGM conditions become preferentially cooler, more diffuse, and lower metallicity (Figure 10).
3. For all galaxies in the M+M sample, there are two prominent temperature phases that comprise >94% of the CGM mass.

(a) The warm phase ($10^{4.5} < T < 10^{5.5}$K) constitutes the majority of CGM mass ($\sim$75%) for 50/64 galaxies in the M+M sample (Figure 8). This phase traces the virial temperature of the halo and exists primarily in the outer regions at $r/R_{200c} \geqslant 0.5$. In terms of metal retention, the warm phase harbors between 5% and 10% of all metals produced by the dwarf galaxy (Figure 9).

(b) The cool phase ($10^{3.8} < T < 10^{4.5}$ K) tends to comprise $\sim$25% of the CGM mass, except at the low virial masses, $M_{200c} < 10^{9.9} M_{\odot}$. At the low mass end, the virial temperature of the halo approaches $T \sim 10^{4.5}$ K, resulting in $\sim$100% of CGM mass being within the cool phase. For $M_{200c} > 10^{9.9}\,M_{\odot}$ galaxies, the cool phase exists in the inner regions of the halo $r \leqslant 0.5 R_{\rm vir}$. It represents the primarily photoionized phase where H I and low metal ions' ionization fractions are greatest in the CGM. The cool phase tends to harbor between 5% and 10% of all metals produced by the dwarf galaxy (Figure 9), notably a comparable fraction to the warm phase.

Our work is focused on the $z = 0$ simulated universe and useful in comparing a large sample of simulated dwarf galaxies to local observations. Future work can expand upon this study by including a range of redshifts and comparing to more observational work, such as N. Mishra et al. (2024) and S. Dutta et al. (2025). Additionally, studies investigating the properties of O VI, how this ion relates to dwarf galaxy activity, and, more generally, how the CGM of dwarf galaxies depends on the modeling choices built into modern simulations will likely prove useful in advancing our understanding of simulated feedback physics and the baryon cycle in the low-mass regime.

Acknowledgments

We thank Kristen B. W. McQuinn and Iryna S. Butsky for helpful conversations during this work. Resources supporting this work were provided by the NASA High-End Computing (HEC) Program through the NASA Advanced Supercomputing (NAS) Division at Ames Research Center. Some of the simulations were performed using resources made available by the Flatiron Institute. The Flatiron Institute is a division of the Simons Foundation. This work used Stampede2 at the Texas Advanced Computing Center (TACC) through allocation MCA94P018 from the Advanced Cyberinfrastructure Coordination Ecosystem: Services & Support (ACCESS) program, which is supported by U.S. National Science Foundation grant Nos. 2138259, 2138286, 2138307, 2137603, and 2138296. D. R.P and A.M.B are supported by NASA grant No. 80NSSC24K0894. A.M.B acknowledges support by grant FI-CCA-Research-00011826 from the Simons Foundation. J.W. is supported by a grant from National Science and Engineering Research Council (NSERC) Canada. C.C. was supported by the NSF under CAREER grant AST-1848107, and this work was performed in part at Aspen Center for Physics, which is supported by NSF grant No. PHY-2210452. N.N.S. was supported by the National Science Foundation MPS-Ascend award ID 2212959.

Appendix A
Individual Halo Properties in the M+M Sample

For this study, the M+M sample is comprised of 64 simulated galaxies, and for most of the analysis we average over multiple galaxies in a given mass bin. In this appendix, we provide various properties for each individual simulated galaxy to support future work that aims to compare with our study. For each galaxy identified by its ID, Table 3 lists the stellar mass; virial mass; virial radius and specific star formation over the last 100 Myr; total gas inside R_{200c}; total disk HI and helium gas mass; total gas in the CGM; total gas mass in the cool and warm phase; total metal mass in the CGM; and average mass weighted gas number density and temperature of the CGM.

Table 3
Individual Halo Properties in the M + M **Sample**

ID	M_*	M_{200c}	R_{200c}	sSFR_{100}	$M_{\mathrm{Gas}}^{\mathrm{Halo}}$	$M_{\mathrm{HI+He}}^{\mathrm{Disk}}$	$M_{\mathrm{Gas}}^{\mathrm{CGM}}$	$M_{\mathrm{Cool}}^{\mathrm{CGM}}$	$M_{\mathrm{Warm}}^{\mathrm{CGM}}$	M_{Z}^{CGM}	ρ_{CGM}	T_{CGM}
r468-1	9.09	10.85	87.04	−9.54	9.67	8.86	9.45	9.27	8.93	7.39	−3.86	4.41
r568-1	9.06	10.82	84.93	−9.46	9.7	9.26	9.22	8.69	9.04	6.91	−4.07	4.69
rogue-1	8.99	10.92	87.59	−9.78	9.55	8.64	9.39	8.95	9.15	7.15	−3.96	4.69
r442-1	8.95	10.89	90.11	−9.42	9.86	9.35	9.48	9.0	9.27	7.0	−3.83	4.7
r502-1	8.93	10.87	88.74	−9.28	9.77	9.08	9.5	9.19	9.18	7.2	−3.87	4.58
r492-1	8.85	10.87	88.74	−9.33	9.86	9.47	9.4	8.91	9.2	6.87	−3.99	4.74
r515-1	8.82	10.9	90.73	−9.38	9.94	9.56	9.48	9.02	9.26	6.92	−3.82	4.69
r556-1	8.81	10.74	80.12	−9.52	9.52	8.92	9.19	8.89	8.86	6.99	−4.14	4.56
r555-1	8.72	10.75	81.02	−9.49	9.57	8.91	9.26	8.92	8.97	6.91	−3.99	4.57
r544-1	8.68	10.82	85.32	−9.24	9.72	9.29	9.3	8.57	9.19	6.59	−4.19	4.8
r489-1	8.68	10.83	85.76	−9.18	9.81	9.29	9.47	8.94	9.29	6.74	−3.92	4.72
storm-1	8.67	10.88	85.04	−9.31	9.82	9.38	9.44	8.92	9.26	6.7	−3.84	4.75
r656-1	8.54	10.69	76.86	−9.6	9.45	8.95	9.08	8.47	8.93	6.6	−4.24	4.72
r613-1	8.52	10.76	81.25	−9.53	9.62	9.14	9.28	8.71	9.12	6.62	−4.15	4.73
r597-1	8.52	10.73	79.67	−9.64	9.51	9.03	9.14	8.5	9.0	6.57	−4.25	4.76
r523-1	8.51	10.78	82.34	−9.59	9.59	9.06	9.26	8.53	9.14	6.53	−4.2	4.82
r642-1	8.47	10.7	77.69	−9.56	9.66	9.2	9.26	8.75	9.06	6.62	−4.08	4.7
r569-1	8.46	10.72	78.99	−9.6	9.63	9.14	9.26	8.7	9.09	6.6	−4.06	4.73
r918-1	8.45	10.76	81.14	−9.8	9.74	9.02	9.53	9.28	9.14	6.78	−3.57	4.49
r634-1	8.43	10.69	77.26	−9.56	9.61	9.11	9.23	8.69	9.06	6.54	−4.04	4.69
r618-1	8.42	10.7	77.44	−9.56	9.44	8.67	9.22	8.79	8.99	6.69	−4.12	4.64
r571-1	8.42	10.78	82.79	−9.75	9.67	9.26	9.14	8.19	9.06	6.22	−4.28	4.83
r614-1	8.41	10.71	78.46	−9.68	9.56	9.11	9.1	8.48	8.95	6.46	−4.19	4.73
r563-1	8.39	10.7	77.72	−9.43	9.53	8.8	9.3	8.84	9.09	6.68	−4.04	4.66
r886-1	8.37	10.63	73.71	−9.39	9.49	8.91	9.18	8.69	8.99	6.52	−4.08	4.64
r552-1	8.36	10.7	77.64	−9.55	9.59	9.11	9.24	8.72	9.05	6.55	−4.09	4.69
elektra-1	8.17	10.62	69.59	−9.69	9.35	8.65	9.11	8.34	9.02	6.11	−4.21	4.78
r718-1	8.02	10.59	71.27	−10.01	9.31	8.68	8.93	8.24	8.81	5.98	−4.32	4.7
storm-2	7.98	10.55	65.73	−9.88	9.55	8.73	9.38	9.19	8.93	6.25	−3.59	4.43
r761-1	7.91	10.56	69.84	−9.57	9.48	9.04	9.02	8.48	8.85	5.85	−4.16	4.67
r916-1	7.85	10.43	63.29	−9.63	9.02	8.3	8.78	8.13	8.65	6.04	−4.4	4.68
r552-2	7.84	10.49	65.9	−10.1	8.94	8.32	8.62	7.46	8.58	5.77	−4.67	4.77
rogue-3	7.84	10.33	55.55	−9.79	9.21	8.7	8.74	8.45	8.43	5.68	−3.83	4.49
r852-1	7.83	10.5	66.59	−9.77	9.03	8.1	8.88	8.06	8.79	5.92	−4.43	4.74
r753-1	7.81	10.46	64.5	−10.13	8.91	8.26	8.62	7.56	8.57	5.76	−4.65	4.73
r850-1	7.78	10.46	64.41	−9.7	8.99	8.03	8.83	8.18	8.7	5.97	−4.39	4.68
r977-1	7.73	10.41	62.17	−10.19	9.0	8.47	8.58	7.73	8.5	5.49	−4.65	4.69
rogue-8	7.71	10.12	47.22	−10.12	8.67	7.93	8.37	7.8	8.23	5.47	−4.41	4.67
elektra-2	7.64	10.46	61.62	−9.33	9.24	8.34	9.07	8.59	8.88	5.69	−3.89	4.59
r753-2	7.64	10.31	57.4	−9.68	8.97	8.26	8.72	8.44	8.38	5.92	−4.35	4.54
r918-2	7.61	10.44	63.52	−9.97	9.22	8.6	8.81	7.99	8.73	5.52	−4.35	4.66
elektra-4	7.56	10.28	53.66	−10.35	8.51	7.41	8.38	7.4	8.33	5.32	−4.64	4.71
storm-4	7.56	10.23	51.38	−10.22	8.72	7.95	8.42	7.43	8.37	5.36	−4.57	4.77
r1023-2	7.52	10.17	51.82	−10.35	8.43	7.61	8.19	8.03	7.66	5.66	−4.67	4.47
cptmarvel-1	7.51	10.19	50.04	−10.04	8.54	7.75	8.34	7.5	8.27	5.24	−4.64	4.63
storm-3	7.37	10.39	58.1	−9.54	9.25	8.6	8.97	8.41	8.83	5.31	−4.08	4.63
rogue-7	7.37	10.17	49.16	−10.15	8.67	7.84	8.44	7.83	8.31	5.33	−4.4	4.63
elektra-5	7.37	10.19	49.84	−9.66	8.84	7.96	8.67	8.0	8.57	5.38	−4.24	4.61
r977-2	7.36	10.25	55.17	−9.89	8.71	7.85	8.52	8.14	8.26	5.6	−4.43	4.56
rogue-10	7.14	10.05	44.96	−10.35	8.2	7.19	8.04	6.77	8.01	4.68	−4.77	4.97
r544-2	7.07	10.11	49.37	−9.88	8.57	7.73	8.38	7.91	8.19	5.29	−4.58	4.56
storm-8	7.02	9.9	40.04	−10.3	8.21	7.09	8.09	7.81	7.77	5.04	−4.54	4.5
storm-7	6.99	9.9	40.15	−10.59	8.14	6.99	8.04	7.24	7.96	4.73	−4.7	4.59
cptmarvel-2	6.95	9.99	43.04	−9.77	8.79	8.14	8.38	8.02	8.12	4.85	−4.17	4.47
rogue-12	6.92	9.88	39.45	−10.23	8.05	7.38	7.73	6.9	7.65	4.61	−4.88	4.84
storm-5	6.9	9.98	42.67	−10.17	8.33	7.2	8.19	7.6	8.06	4.93	−4.59	4.57
cptmarvel-5	6.86	9.88	39.26	−10.26	8.08	7.2	7.86	7.58	7.52	4.66	−4.78	4.51
cptmarvel-6	6.84	9.82	37.59	−10.39	8.13	6.99	7.97	7.75	7.57	4.79	−4.61	4.48
cptmarvel-3	6.71	9.94	41.33	−9.61	8.61	7.84	8.27	7.88	8.04	4.74	−4.38	4.52
rogue-11	6.67	9.91	40.27	−9.83	8.44	7.69	8.16	7.43	8.06	4.57	−4.56	4.58
r761-4	6.55	9.71	36.31	−10.09	8.09	7.43	7.71	7.69	6.15	4.74	−4.69	4.27
storm-6	6.52	9.93	40.82	−9.24	8.45	7.4	8.3	7.86	8.1	4.83	−4.37	4.52
r571-2	6.38	9.84	40.18	−9.79	8.12	7.11	7.98	7.92	7.06	4.86	−4.71	4.42
r556-3	6.3	9.7	36.0	−9.72	8.39	7.81	8.0	7.94	7.15	4.55	−4.48	4.4

Note. The columns, from left to right, list each galaxy's simulation volume name and halo id (ID), stellar mass (M_*), virial mass (M_{200c}), virial radius (R_{200c}) in units of kiloparsecs, specific star formation over the last 100 Myr (sSFR_{100}) in units of per year, total gas inside R_{200c} ($M_{\mathrm{Gas}}^{\mathrm{Halo}}$), H I and helium gas mass in the disk defined using $r_{\Sigma_{\mathrm{HI}}}$ ($M_{\mathrm{HI+He}}^{\mathrm{Disk}}$), total gas in the CGM defined as $0.15 < r/R_{200c} < 1$, ($M_{\mathrm{Gas}}^{\mathrm{Halo}}$), total gas mass in the cool phase ($M_{\mathrm{Cool}}^{\mathrm{CGM}}$), total gas mass in the warm phase ($M_{\mathrm{Warm}}^{\mathrm{CGM}}$), total metal mass in the CGM ($M_{\mathrm{Z}}^{\mathrm{CGM}}$), average mass-weighted gas number density in the CGM (ρ_{CGM}) in units of cubic centimeters, and average mass-weighted gas temperature in the CGM T_{CGM} in units of kelvins. All masses are provided in solar masses ($M_\odot$), and all values, except R_{200c}, are provided as logarithms.

Appendix B
Marvel versus Massive Comparison

Figures 13 and 14 show column density profiles in a similar format to Figures 4 and 5, where each column presents data for a given stellar mass bin (denoted at the top) and each row presents the column densities in a specific ion (denoted in the top left of each panel). In these figures, we show the median column densities for each galaxy in the M + M sample and differentiate between suites. Specifically, red lines are profiles for galaxies in the Marvel-ous Dwarfs suite, and blue lines are profiles for galaxies in the Marvelous Massive Dwarfs suite. We find little clear variation between suites, but note that the two suites are biased toward higher or lower masses (Figure 1), and Marvel galaxies tend to span a larger range in column densities. The stellar mass range $M_* = 10^{7.5-8.5}\,M_\odot$ has the most overlap and a comparable number of galaxies across the two suites, with eight and 21 from Marvel and Massive, respectively. When comparing the median of each suite in this mass range, we find that the medians are within 1σ of one another, across impact parameters and ions—except for $N_{\rm OVI}$. Median $N_{\rm OVI}$ values tend to be within 1–1.5σ, and the Massive suite produces greater column densities. The minor differences seen in column densities may be due to the buoyancy of SB versus BW (see B. W. Keller et al. 2020), or the fact that the SB model used here adopts a smaller $E_{\rm SN}$ than the BW model. Understanding the nuances is left to future work. However, we conclude that the overall differences between the two runs are minor, justifying our use of both suites to span a broader mass range and increase our sample size.

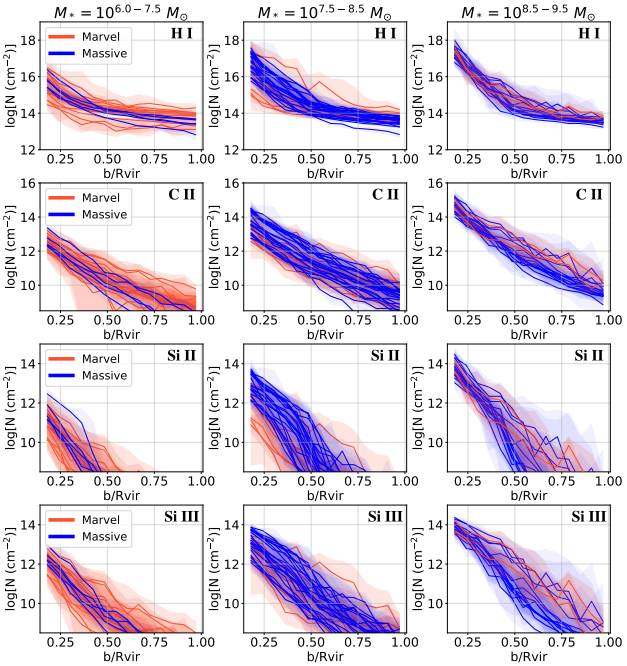

Figure 13. Column density profiles for all galaxies in the M + M sample. Each panel shows the median column density profiles in a given ion around a galaxy within the stellar mass bin, denoted at the top of the figure. Each line represents the profile for a single galaxy, color-coded red if the galaxy is from the Marvel suite or blue if the galaxy is from the Massive suite. Also shown is the 16th–84th percentile range for a given galaxy. We find that the overall differences between the two suites are minor.

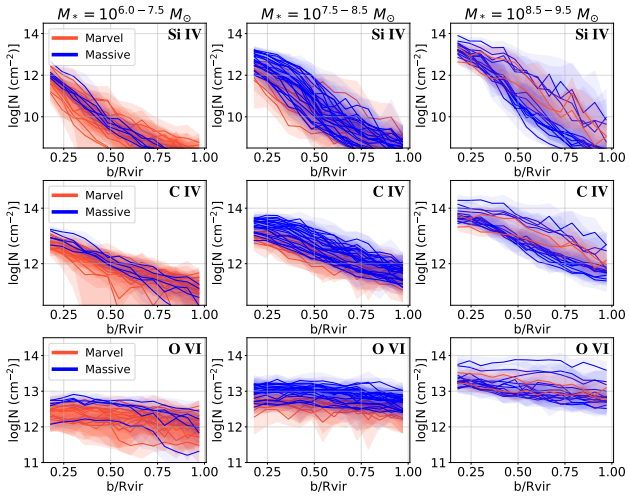

Figure 14. Same as Figure 13 but for Si IV, C IV, and O VI.

Appendix C
Consequences of $15R_{200c}$ CGM Definition

While analyzing the CGM in the M + M sample, we opted to define the CGM as a fixed fraction of the viral radius ($0.15R_{200c}$) to remove the disk of the galaxy and define the disk according to $r_{\Sigma_{\rm HI}}$. We argue that the CGM definition enables better comparison to past work and observations and attempts to normalize our calculations by the gravitational influence of the galaxies. Additionally, we argue our choice of $r_{\Sigma_{\rm HI}}$ is more similar to how an observer would select the gaseous disk of a galaxy. However, it is a fact that, given the range in masses utilized, the physical extent of our halos differs by a factor of $\sim 2\times$ from the low- to the high-mass end. Therefore, we are selecting different physical volumes when we utilize the virial radius. In this section, we quantify the fraction of the halo that we remove when we implement these definitions.

Figure 15 shows the relation between the virial radius of a halo and the approximate size of the disk according to the radius at which the surface density of H I falls below 1.0 $M_\odot\,{\rm pc}^{-2}$ (the definition adopted for $r_{\Sigma_{\rm HI}}$ in the paper) and 0.5 $M_\odot\,{\rm pc}^{-2}$ and the radius within which 90% of the starlight is contained. Solid lines show the median values, and shaded regions show the 16th–84th percentile range. Figure 15 provides insight into the extent of the galaxy (both its ISM and stellar component) compared to the halo size as seen by a mock observer. We find the size of the galaxy decreases relative to R_{200c} with decreasing mass. For the highest-mass galaxies ($\log(M_*/M_\odot) > 8.5$), the $r \geqslant 0.15R_{200c}$ CGM definition removes the ISM and stellar component plus $\sim$5% of the halo. This is done to focus our study on the extended CGM. However, for the lowest-mass galaxies, the fraction removed beyond the disk and from the CGM rises to $\sim$10%. The consequence of this is that we remove the coolest and densest material outside of the disk that may be considered CGM gas by an observer. This fact likely drives the mass dependence seen in the left column of Figure 10, where with declining mass we see the cool, dense component disappear from the CGM region. Additionally, given the trend of increasing column densities for decreasing impact parameter in

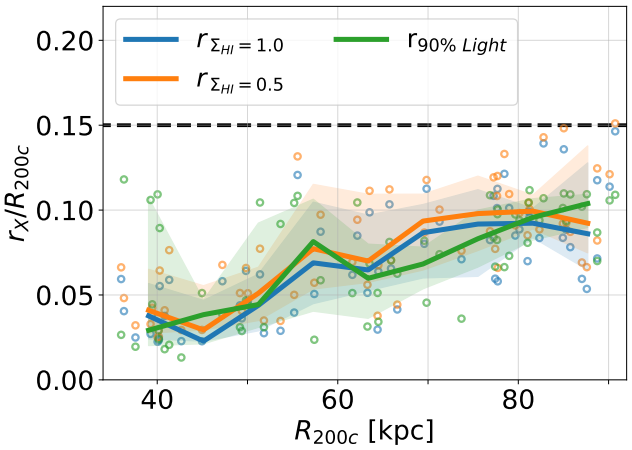

Figure 15. Fractional extent of the galaxy disk based on three different definitions: the radius at which the surface density of H I falls below 1.0 $M_\odot$ pc^{-2} ($r_{\Sigma_{\rm HI}=1.0}$; blue, the same definition used for $r_{\Sigma_{\rm HI}}$), the radius at which the surface density of H I falls below 0.5 $M_\odot$ pc^{-2} ($r_{\Sigma_{\rm HI}=0.5}$; orange), and the radius within which 90% of the starlight is contained ($r_{90\%\rm Light}$; green). Solid lines show the median values, shaded regions encompass the 16th–84th percentile range, and individual halos are shown as points.

Figures 4 and 5, there are likely observable metals within $0.15R_{200c}$ or 6 kpc for $\log(M_*/M_\odot) < 7.5$ galaxies.

ORCID iDs

Daniel R. Piacitelli https://orcid.org/0000-0003-0200-6986
Alyson M. Brooks https://orcid.org/0000-0002-0372-3736
Charlotte Christensen https://orcid.org/0000-0001-6779-3429
N. Nicole Sanchez https://orcid.org/0000-0001-7589-6188
Yakov Faerman https://orcid.org/0000-0003-3520-6503
Sijing Shen https://orcid.org/0000-0001-8523-1171
Akaxia Cruz https://orcid.org/0000-0001-7831-4892
Ben Keller https://orcid.org/0000-0002-9642-7193
Thomas R. Quinn https://orcid.org/0000-0001-5510-2803

References

Asplund, M., Grevesse, N., Sauval, A. J., & Scott, P. 2009, ARA&A, 47, 481
Augustin, R., Péroux, C., Hamanowicz, A., et al. 2021, MNRAS, 505, 6195
Azartash-Namin, B., Engelhardt, A., Munshi, F., et al. 2024, ApJ, 970, 40
Baumschlager, B., Shen, S., & Wadsley, J. W. 2024, A&A, 691, A219
Baumschlager, B., Shen, S., & Wadsley, J. W. 2025, arXiv:2508.19396
Bellovary, J. M., Hayoune, S., Chafla, K., et al. 2021, MNRAS, 505, 5129
Bordoloi, R., Prochaska, J. X., Tumlinson, J., et al. 2018, ApJ, 864, 132
Bordoloi, R., Tumlinson, J., Werk, J. K., et al. 2014, ApJ, 796, 136
Brooks, A. M., Governato, F., Quinn, T., Brook, C. B., & Wadsley, J. 2009, ApJ, 694, 396
Burchett, J. N., Tripp, T. M., Bordoloi, R., et al. 2016, ApJ, 832, 124
Butsky, I. S., Werk, J. K., Tchernyshyov, K., et al. 2022, ApJ, 935, 69
Chevalier, R. A. 1974, ApJ, 188, 501
Christensen, C., Quinn, T., Governato, F., et al. 2012, MNRAS, 425, 3058
Christensen, C. R., Brooks, A. M., Munshi, F., et al. 2024, ApJ, 961, 236
Christensen, C. R., Davé, R., Brooks, A., Quinn, T., & Shen, S. 2018, ApJ, 867, 142
Christensen, C. R., Davé, R., Governato, F., et al. 2016, ApJ, 824, 57
Cook, A. W. S., van de Voort, F., Pakmor, R., & Grand, R. J. J. 2025, MNRAS, 543, 1224
Cowie, L. L., & McKee, C. F. 1977, ApJ, 211, 135
Dalcanton, J. J. 2007, ApJ, 658, 941
Davé, R. 2009, in ASP Conf. Ser. 419, Galaxy Evolution: Emerging Insights and Future Challenges, ed. S. Jogee et al. (San Francisco, CA: ASP), 347
Deg, N., Arora, N., Spekkens, K., et al. 2024, ApJ, 976, 159
Dutta, S., Muzahid, S., Schaye, J., et al. 2025, ApJ, 985, 44
Faerman, Y., Zheng, Y., & Oppenheimer, B. D. 2025, ApJL, 982, L30
Faucher-Giguère, C.-A. 2020, MNRAS, 493, 1614
Ferland, G. J., Chatzikos, M., Guzmán, F., et al. 2017, RMxAA, 53, 385
Gutcke, T. A., Stinson, G. S., Macciò, A. V., Wang, L., & Dutton, A. A. 2017, MNRAS, 464, 2796
Haardt, F., & Madau, P. 2012, ApJ, 746, 125
Hafen, Z., Faucher-Giguère, C.-A., Anglés-Alcázar, D., et al. 2019, MNRAS, 488, 1248
Hsu, W. H., Putman, M. E., Heitsch, F., et al. 2011, AJ, 141, 57
Hummels, C. B., Smith, B. D., Hopkins, P. F., et al. 2019, ApJ, 882, 156
Hummels, C. B., Smith, B. D., & Silvia, D. W. 2017, ApJ, 847, 59
Ji, S., Chan, T. K., Hummels, C. B., et al. 2020, MNRAS, 496, 4221
Johnson, S. D., Chen, H.-W., & Mulchaey, J. S. 2015, MNRAS, 449, 3263
Johnson, S. D., Chen, H.-W., Mulchaey, J. S., Schaye, J., & Straka, L. A. 2017, ApJL, 850, L10
Karachentsev, I. D., Makarov, D. I., & Kaisina, E. I. 2013, AJ, 145, 101
Keith, B., Munshi, F., Brooks, A. M., et al. 2025, ApJ, 986, 138
Keller, B. W., Kruijssen, J. M. D., & Wadsley, J. W. 2020, MNRAS, 493, 2149
Keller, B. W., Wadsley, J., Benincasa, S. M., & Couchman, H. M. P. 2014, MNRAS, 442, 3013
Keller, B. W., Wadsley, J., & Couchman, H. M. P. 2016, MNRAS, 463, 1431
Kroupa, P. 2001, MNRAS, 322, 231
Lee, J. C., Gil de Paz, A., Kennicutt, R. C., Jr., et al. 2011, ApJS, 192, 6
Li, F., Rahman, M., Murray, N., et al. 2021, MNRAS, 500, 1038
Liang, C. J., & Chen, H.-W. 2014, MNRAS, 445, 2061
Lin, Y.-H., Scarlata, C., Mehta, V., et al. 2023, ApJ, 951, 138
McConnachie, A. W. 2012, AJ, 144, 4
McCourt, M., Oh, S. P., O'Leary, R., & Madigan, A.-M. 2018, MNRAS, 473, 5407
McQuinn, K. B. W., Skillman, E. D., Dolphin, A., et al. 2015, ApJL, 815, L17
McQuinn, K. B. W., Berg, D. A., Skillman, E. D., et al. 2020, ApJ, 891, 181
Menon, H., Wesolowski, L., Zheng, G., et al. 2015, ComAC, 2, 1
Mina, M., Shen, S., Keller, B. W., et al. 2021, A&A, 655, A22
Mishra, N., Johnson, S. D., Rudie, G. C., et al. 2024, ApJ, 976, 149
Munshi, F., Brooks, A. M., Applebaum, E., et al. 2021, ApJ, 923, 35
Munshi, F., Governato, F., Brooks, A. M., et al. 2013, ApJ, 766, 56
Muratov, A. L., Kereš, D., Faucher-Giguère, C.-A., et al. 2017, MNRAS, 468, 4170
Nelson, D., Kauffmann, G., Pillepich, A., et al. 2018, MNRAS, 477, 450
Nelson, D., Sharma, P., Pillepich, A., et al. 2020, MNRAS, 498, 2391
Obreja, A., Macciò, A. V., Moster, B., et al. 2019, MNRAS, 490, 1518
Onorbe, J., Garrison-Kimmel, S., Maller, A. H., et al. 2013, MNRAS, 437, 1894
Pace, A. B. 2025, OJAp, 8, 142
Peeples, M. S., Corlies, L., Tumlinson, J., et al. 2019, ApJ, 873, 129
Planck Collaboration, Ade, P. A. R., Aghanim, N., et al. 2016, A&A, 594, A13
Pontzen, A., Roškar, R., Stinson, G. S., et al. 2013, pynbody: Astrophysics Simulation Analysis for Python, Astrophysics Source Code Library, ascl:1305.002
Qu, Z., & Bregman, J. N. 2022, ApJ, 927, 228
Qu, Z., Chen, H.-W., Johnson, S. D., et al. 2024, ApJ, 986, 8
Raiteri, C. M., Villata, M., & Navarro, J. F. 1996, A&A, 315, 105
Ramesh, R., & Nelson, D. 2024, MNRAS, 528, 3320
Ramesh, R., Nelson, D., & Girichidis, P. 2025, A&A, 699, A125
Rey, M. P., Katz, H. B., Cameron, A. J., Devriendt, J., & Slyz, A. 2024, MNRAS, 528, 5412
Riggs, C. L., Brooks, A. M., Munshi, F., et al. 2024, ApJ, 977, 20
Roca-Fàbrega, S., Dekel, A., Faerman, Y., et al. 2019, MNRAS, 484, 3625
Ruan, D., Brooks, A. M., Cruz, A., et al. 2025, MNRAS, 541, 2180
Sanchez, N. N., Tremmel, M., Werk, J. K., et al. 2021, ApJ, 911, 116
Sanchez, N. N., Werk, J. K., Tremmel, M., et al. 2019, ApJ, 882, 8
Sanchez, N. N., Werk, J. K., Christensen, C., et al. 2024, ApJ, 967, 100
Sharma, R. S., Brooks, A. M., Somerville, R. S., et al. 2020, ApJ, 897, 103
Shen, S., Wadsley, J., & Stinson, G. 2010, MNRAS, 407, 1581
Spergel, D. N., Bean, R., Doré, O., et al. 2007, ApJS, 170, 377
Stern, J., Faucher-Giguère, C.-A., Fielding, D., et al. 2021, ApJ, 911, 88
Stinson, G., Seth, A., Katz, N., et al. 2006, MNRAS, 373, 1074
Stopyra, S., Pontzen, A., Peiris, H., Roth, N., & Rey, M. P. 2021, ApJS, 252, 28
Taira, E., Kopenhafer, C., Oshea, B. W., et al. 2025, ApJ, 991, 221
Tchernyshyov, K., Werk, J. K., Wilde, M. C., et al. 2022, ApJ, 927, 147
Thielemann, F. K., Nomoto, K., & Yokoi, K. 1986, A&A, 158, 17
Tremmel, M., Karcher, M., Governato, F., et al. 2017, MNRAS, 470, 1121

Tumlinson, J., Peeples, M. S., & Werk, J. K. 2017, ARA&A, 55, 389
Tung, P.-C., & Chen, K.-J. 2025, ApJ, 988, 127
Turk, M. J., Smith, B. D., Oishi, J. S., et al. 2011, ApJS, 192, 9
van de Voort, F., & Schaye, J. 2012, MNRAS, 423, 2991
van de Voort, F., Springel, V., Mandelker, N., van den Bosch, F. C., & Pakmor, R. 2019, MNRAS, 482, L85
Wadsley, J. W., Keller, B. W., & Quinn, T. R. 2017, MNRAS, 471, 2357
Wadsley, J. W., Stadel, J., & Quinn, T. 2004, NewA, 9, 137
Weidemann, V. 1987, A&A, 188, 74
Wyder, T. K., Martin, D. C., Schiminovich, D., et al. 2007, ApJS, 173, 293
Zahedy, F. S., Chen, H.-W., Johnson, S. D., et al. 2019, MNRAS, 484, 2257
Zheng, Y., Faerman, Y., Oppenheimer, B. D., et al. 2024, ApJ, 960, 55